Analyzing radial flow features in p-Pb and p-p collisions at several TeV by studying identified-particle production with the event generator EPOS3

K. Werner,[1] B. Guiot,[1] Iu. Karpenko,[2,3] and T. Pierog[4]
[1]*SUBATECH, University of Nantes-IN2P3/CNRS-EMN, Nantes, France*
[2]*Bogolyubov Institute for Theoretical Physics, Kiev 143, 03680, Ukraine*
[3]*FIAS, Johann Wolfgang Goethe Universitaet, Frankfurt am Main, Germany*
[4]*Karlsruhe Institute of Technology, KIT, Campus North, Institute für Kernphysik, Karlsruhe, Germany*
(Received 7 December 2013; revised manuscript received 28 April 2014; published 9 June 2014)

Experimental transverse momentum spectra of identified particles in p-Pb collisions at 5.02 TeV show many similarities to the corresponding Pb-Pb results, the latter ones usually being interpreted in terms of hydrodynamic flow. We analyze these data using EPOS3, an event generator based on a 3D + 1 viscous hydrodynamical evolution starting from flux-tube initial conditions, which are generated in the Gribov-Regge multiple scattering framework. An individual scattering is referred to as Pomeron, identified with a parton ladder, eventually showing up as flux tubes (or strings). Each parton ladder is composed of a perturbative QCD hard process, plus initial- and final-state linear parton emission. Nonlinear effects are considered by using saturation scales Q_s, depending on the energy and the number of participants connected to the Pomeron in question. We compute transverse momentum (p_t) spectra of pions, kaons, protons, lambdas, and Ξ baryons in p-Pb and p-p scattering, compared to experimental data and many other models. In this way we show in a quantitative fashion that p-Pb data (and even p-p ones) show the typical "flow effect" of enhanced particle production at intermediate p_t values, more and more visible with increasing hadron mass.

DOI: 10.1103/PhysRevC.89.064903 PACS number(s): 25.75.Ld, 47.75.+f

I. INTRODUCTION

Collective hydrodynamic flow seems to be well established in heavy-ion (HI) collisions at energies between 200 and 2760 A GeV, whereas p-p and p-nucleus (p-A) collisions are often considered to be simple reference systems, showing "normal" behavior, such that deviations in HI collisions with respect to p-p or p-A reveal "new physics." Surprisingly, the first results from p-Pb at 5.02 TeV on the transverse momentum dependence of azimuthal anisotropies and particle yields are very similar to the observations in HI scattering. In this paper we focus on transverse momentum spectra of identified particles. The CMS Collaboration showed recently [1] that the shapes of transverse momentum spectra of pions, kaons, and protons change in a characteristic way with multiplicity, which looks like an increasing contribution from radial flow with multiplicity. A similar conclusion can be drawn from recent measurements from ALICE [2] concerning transverse momentum spectra of pions, kaons, protons, and lambdas. In particular, the ratio lambda over kaon shows a peak structure, similar to that in HIs, more and more pronounced with increasing multiplicity.

Do we see radial flow in p-Pb collisions? To answer this question, we employ the EPOS3 approach, well suited for this problem, because it provides within a unique theoretical scheme the initial conditions for a hydrodynamical evolution in p-p, p-A, and HI collisions. The initial conditions are generated in the Gribov-Regge multiple scattering framework. An individual scattering is referred to as Pomeron, identified with a parton ladder, eventually showing up as flux tubes (also called strings). Each parton ladder is composed of a perturbative QCD (pQCD) hard process, plus initial- and final-state linear parton emission. Our formalism is referred to as "parton-based Gribov Regge theory" and described in detail in Ref. [3]. Based on these initial conditions, we performed already ideal hydrodynamical calculations [4–7] to analyze HI and p-p scattering at the BNL Relativistic Heavy Ion Collider (RHIC) and CERN Large Hadron Collider (LHC). In this paper we discuss two major improvements: a more sophisticated treatment of nonlinear effects in the parton evolution by considering individual (per Pomeron) saturation scales and a 3D + 1 viscous hydrodynamical evolution. There are also changes in our core-corona procedure, which amounts to separating the initial energy of the flux tubes into a part which constitutes the initial conditions for hydro (core) and the particles which leave the "matter." This is crucial as well in proton-nucleus collisions (as in all other collision types).

To understand the results discussed later in this paper, we show in Fig. 1 the effect of flow on identified-particle spectra by comparing p_t distributions from pure string decay to spectra from a pure hydrodynamic evolution. In case of string fragmentation, heavier particles are strongly suppressed compared to lighter ones, but the shapes are not so different. This picture changes completely in the fluid case: The heavier the particle, the more it gets shifted from low to intermediate p_t. This is a direct consequence of the fact that the particles are produced from fluid cells characterized by radial flow velocities, which gives more transverse momentum to heavier particles.

There are few other studies of hydrodynamic expansion in proton-nucleus systems. In Ref. [8], fluctuating initial conditions based on the so-called Monte Carlo Glauber model (which is actually a wounded nucleon model) are employed, followed by a viscous hydrodynamical evolution. Also, Ref. [9] uses fluctuating initial conditions, here based on both Glauber Monte Carlo and Glasma initial conditions. Finally in Ref. [10], ideal hydrodynamical calculations are performed, starting from smooth Glauber model initial conditions.

 ©2014 American Physical Society

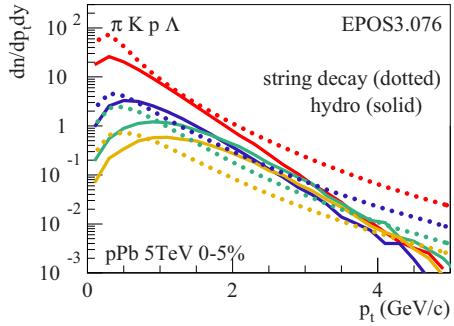

FIG. 1. (Color online) Identified-particle spectra as a function of p_t, for central (0%–5%) p-Pb collisions at 5.02 TeV. We show results for particle production from string decay, i.e., EPOS without hydro (dotted curves), and particle production from pure hydro, without corona (solid lines). In both cases, we show (from top to bottom) pions, kaons, protons, and lambdas.

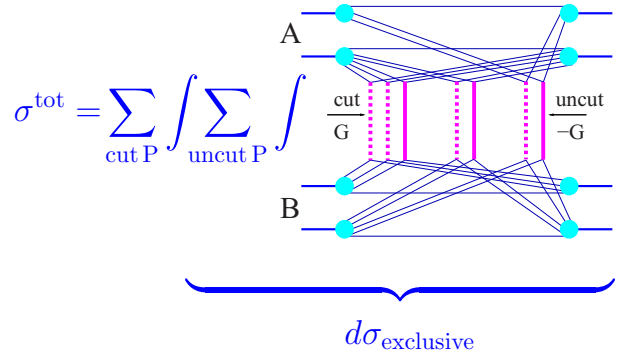

FIG. 2. (Color online) The total cross section expressed in terms of cut (dashed lines) and uncut (solid lines) Pomerons, for nucleus-nucleus, proton-nucleus, and proton-proton collisions. Partial summations make it possible to obtain exclusive cross sections.

In Secs. II to VII, we discuss the different elements of the EPOS3 model. In Secs. VIII to X, we report results on p-Pb and p-p scattering, comparing EPOS3 with data and other models, which leads to conclusions concerning hydrodynamical flow. Data points are systematically shown with statistical errors only, unless mentioned otherwise (often the error bars are too small to be visible). When comparing simulations to data, we always adopt the same multiplicity definition as in experiment.

II. MULTIPLE POMERON EXCHANGE AND SATURATION

The starting point is a multiple scattering approach corresponding to a marriage of Gribov-Regge theory [11–21] and pQCD, which has the advantage of being applicable to deep inelastic lepton-proton scattering, as well as proton-proton (p-p), proton-nucleus (p-A), and nucleus-nucleus (A-A) collisions (see Ref. [3]). A very important aspect of this formalism is its ability to provide **exclusive** cross sections, a necessary requirement for Monte Carlo applications, the latter ones becoming more and more popular after the discovery of the importance of event-by-event fluctuations, even in A-A collisions.

Gribov-Regge theory starts from the hypothesis that the T matrix of the scattering process can be written as a product of elementary objects (later) referred to as Pomerons ($\mathbb{P}$'s). In Ref. [3], we generalize the approach by adding energy-momentum conservation into the expression for the T matrix. Squaring the T matrix can be done conveniently using the Cutcosky cutting rule technique, and one obtains for the total cross section an expression as illustrated in Fig. 2, expressed in terms of cut and uncut Pomerons. The mathematical expressions corresponding to the cut Pomeron is referred to as G (to be discussed later), for the uncut one we have $-G$ (see Ref. [3]).

It is, of course, very useful to have an explicit formula for the total cross section, but the real power of the expression in Fig. 2 is the fact that partial summations (as indicated in the figure) provide exclusive cross sections for subprocesses, as, for example, the cross section for triple scattering (triple-$\mathbb{P}$ exchange) in p-p collisions or the cross section for a given number of $\mathbb{P}$ exchanges in p-A. This discussion is particularly important for p-A scattering, because finally the number of Pomeron exchanges characterizes the geometry of a collision, not the number of participants or the number of collisions.

The following formulas are somewhat simplified, not showing explicitly summations over parton flavors, the precise formulas being given in Ref. [3]. The expression corresponding to Fig. 2 is

$$
\begin{aligned}
\sigma^{\rm tot} = \int d^2b \int \prod_{i=1}^{A} d^2b_i^A\, dz_i^A\, \rho_A\Big[\sqrt{\big(b_i^A\big)^2+\big(z_i^A\big)^2}\Big] \prod_{j=1}^{B} d^2b_j^B\, dz_j^B\, \rho_B\Big[\sqrt{\big(b_j^B\big)^2+\big(z_j^B\big)^2}\Big] \\
\times \sum_{m_1 l_1} \cdots \sum_{m_{AB} l_{AB}} \big(1-\delta_{0\Sigma m_k}\big) \int \prod_{k=1}^{AB} \left(\prod_{\mu=1}^{m_k} dx_{k,\mu}^+ dx_{k,\mu}^- \prod_{\lambda=1}^{l_k} d\tilde{x}_{k,\lambda}^+ d\tilde{x}_{k,\lambda}^- \right) \\
\times \left\{ \prod_{k=1}^{AB} \left[\frac{1}{m_k!}\frac{1}{l_k!} \prod_{\mu=1}^{m_k} G\big(x_{k,\mu}^+, x_{k,\mu}^-, s, |\vec{b}+\vec{b}_{\pi(k)}^A - \vec{b}_{\tau(k)}^B|\big) \prod_{\lambda=1}^{l_k} -G\big(\tilde{x}_{k,\lambda}^+, \tilde{x}_{k,\lambda}^-, s, |\vec{b}+\vec{b}_{\pi(k)}^A - \vec{b}_{\tau(k)}^B|\big) \right] \right. \\
\left. \times \prod_{i=1}^{A} F_{\rm remn}\left(1-\sum_{\pi(k)=i} x_{k,\mu}^+, -\sum_{\pi(k)=i} \tilde{x}_{k,\lambda}^+\right) \prod_{j=1}^{B} F_{\rm remn}\left(1-\sum_{\tau(k)=j} x_{k,\mu}^- - \sum_{\tau(k)=j} \tilde{x}_{k,\lambda}^-\right) \right\}, \qquad (1)
\end{aligned}
$$

where A and B are the number of nucleons of the two nuclei, $(\vec{b}_i^{A/B}, z_i^{A/B})$ the nucleon coordinates, $\rho^{A/B}$ the nuclear densities, $x_{k,\mu}^{+/-}$ and $\tilde{x}_{k,\mu}^{+/-}$ the light cone momentum fractions of, respectively, the cut and uncut Pomerons. The functions $\pi(k)$ and $\tau(k)$ refer to the projectile and target nucleon linked to nucleon-nucleon pair (or "collision number") k, and we use $F_{\text{remn}}(x) = [x\theta(x)\theta(1-x)]^{\alpha}$ with θ being the Heaviside function, which ensures energy conservation. This is the master formula of our approach, because it allows to compute (doing partial summation) exclusive cross-section calculations for particular subprocesses. The formula is also valid for p-p scattering; here we have simply $A = B = 1$ and $\rho_{A/B}(\vec{x}) = \delta(\vec{x})$.

The single Pomeron contribution G is the imaginary part of the transverse Fourier transform of the single Pomeron exchange amplitude T divided by the cms energy $\hat{s}$. The amplitude T is given as a sum over several terms; see Ref. [3]. One contributions is the soft one, T_{soft}, corresponding to a soft Pomeron exchange, parametrized in Regge pole fashion. The most important contribution at high energies is the semihard contribution $T_{\text{sea-sea}}$, with

$$i\,T_{\text{sea-sea}}(\hat{s},t) = \int_0^1 \frac{dz^+}{z^+}\frac{dz^-}{z^-}\,\text{Im}\,T_{\text{soft}}\left(\frac{s_0}{z^+},t\right) \times \text{Im}\,T_{\text{soft}}\left(\frac{s_0}{z^-},t\right) i\,T_{\text{hard}}(z^+z^-\hat{s},t), \tag{2}$$

with the hard scattering amplitude T_{hard} given as

$$T_{\text{hard}} = i\hat{s}\,\sigma_{\text{hard}}(\hat{s})\exp\left(R_{\text{hard}}^2 t\right), \tag{3}$$

and with

$$\begin{aligned}\sigma_{\text{hard}}\left(\hat{s},Q_0^2\right) &= \frac{1}{2\hat{s}}2\text{Im}\,T_{\text{hard}}(\hat{s},t=0)\\ &= K\int dx_B^+ dx_B^- dp_t^2 \frac{d\sigma_{\text{Born}}^{ml}}{dp_t^2}\left(x_B^+x_B^-\hat{s},p_t^2\right)\\ &\quad\times E_{\text{QCD}}\left(x_B^+,Q_0^2,M_F^2\right)E_{\text{QCD}}\left(x_B^-,Q_0^2,M_F^2\right)\\ &\quad\times\theta\left(M_F^2-Q_0^2\right),\end{aligned} \tag{4}$$

based on the fact that the real part of T_{hard} can be neglected and its slope R_{hard}^2 is very small [22,23] (and finally taken to be zero). The functions E_{QCD} represent the linear parton evolution, following the same evolution equations as the usual parton distribution functions, but here the initial condition is $E_{\text{QCD}}(z,Q_0^2,Q_0^2) = \delta(1-z)$. We use $M_F^2 = p_t^2/4$. So far, Q_0 has been a constant, but this will change as discussed below.

In addition to the "sea-sea" contribution as discussed above, we have "val-val," "sea-val," and "val-sea" (see Ref. [3]), where "sea" and "val" refer to sea or valence quarks on respectively the projectile and target side, initiating the parton ladder.

The formula Eq. (4) looks very similar to the usual factorization formula used to compute inclusive cross sections, but here we use it to compute the single Pomeron T matrix.

It is known [3] that our formalism as described so far is incomplete; for example, total cross sections will grow powerlike at high energies, violating the famous Froissart bound. The missing element is an explicit treatment of nonlinear effects concerning the parton evolutions. It is known that parton saturation effects play an important role [24–29] and can be summarized by the so-called saturation scale Q_s, representing the virtuality scale below which nonlinear effects (like gluon-gluon fusion) become important. Popular expressions for the A and x dependence (respectively mass number and longitudinal momentum fraction) are

$$Q_s^2 \sim \frac{A^{1/3}}{x^{\lambda}} \tag{5}$$

or (for the centrality dependence)

$$Q_s^2 \sim \frac{N_{\text{part}}}{x^{\lambda}}, \tag{6}$$

with N_{part} being the number of participating nucleons.

We adapt the above formulas to our formalism and use for each Pomeron

$$Q_s^2 = B_{\text{sat}}\frac{N_{\text{part}}}{(1/\hat{s})^{\lambda}}, \tag{7}$$

where $\hat{s}$ is the cms energy of the Pomeron and N_{part} the number of participants. We use $\lambda = 0.25$. These individual scales Q_s replace the constant values Q_0 in the above formulas. The proportionality constant B_{sat} is chosen to assure binary scaling in p-A and A-A at high p_t.

How does one compute N_{part}? First one might think of estimating simply the number of participating nucleons. For example, for a given Pomeron exchanged between projectile nucleon i and target nucleon j, one counts the projectile nucleons being closer to nucleon j than some transverse distance b_0,

$$N_{\text{part}}^{\text{proj}} = \sum_{\text{proj nucleons } i'} \Theta(b_0 - |\vec{b} + \vec{b}_{i'} - \vec{b}_j|), \tag{8}$$

with $\vec{b}$ being the impact parameter, and $\vec{b}_{i'}$ and $\vec{b}_j$ referring to the transverse positions of the nucleons in the nuclei. A corresponding formula applies for the target participants. We want to go further and estimate the number of participating partons, because we expect already saturation effects in proton-proton scattering. So we use actually

$$N_{\text{part}}^{\text{proj}} = \sum_{\text{proj nucleons } i'} f_{\text{part}}(|\vec{b} + \vec{b}_{i'} - \vec{b}_j|), \tag{9}$$

with

$$f_{\text{part}}(b) = \Theta(b_0 - b)\,g[A_{\text{sat}}\exp(-b^2/4\pi\lambda_{\text{soft}})], \tag{10}$$

where $\exp(-b^2/4\pi\lambda_{\text{soft}})$ is our "usual" b dependence of the single Pomeron amplitudes, with $\lambda_{\text{soft}} = 2R_{\text{part}}^2 + \alpha'_{\text{soft}}\ln(s/s_0)$. Here R_{part} and α'_{soft} are soft Pomeron parameters (see Ref. [3]). The phenomenological function $g(x) = x/[1-\exp(-x)]$ is the average of a Poisson distribution with at least one scattering. We compute correspondingly the number of target participants, and then we define N_{part} to be the maximum of the two numbers $N_{\text{part}}^{\text{proj}}$ and $N_{\text{part}}^{\text{targ}}$.

The effect of the saturation scale can be seen clearly when comparing transverse momentum distributions of primary partons (originating from the hard scattering process) for central and peripheral p-Pb collisions; see Fig. 3. We plot

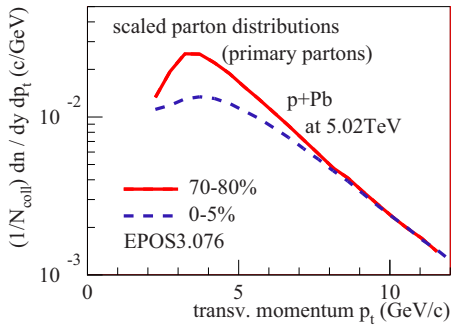

FIG. 3. (Color online) Scaled parton distributions as a function of p_t, for central (0%–5%) and peripheral (70%–80%) p-Pb collisions at 5 TeV.

scaled distributions, i.e., the p-A results divided by the number $N_{\rm coll}$ of binary collisions. Whereas the two curves coincide for large p_t, the low p_t region in the central case is significantly suppressed compared to the peripheral one. In other words, we obtain a different centrality dependence of the parton multiplicity n at low and high p_t:

(i) $n\{\text{high } p_t\}$ grows with $N_{\rm coll}$ (= binary scaling);
(ii) $n\{\text{low } p_t\}$ grows less than $N_{\rm coll}$ (the statement also holds for the integrated multiplicity).

There is considerable confusion about these different scaling behaviors at low and high p_t. It is often referred to as soft and hard contributions, with the soft one scaling as the number of participants (or wounded nucleons). However, this is an old concept from low-energy scattering, where projectile and target fragmentation play a role at midrapidity, which is not at all the case in the TeV energy domain. To be clear: here there is nothing soft, we just have more or less screening at different p_t, governed by the saturation scale.

Introducing a saturation scale to account for nonlinear effects is new in EPOS3, and it replaces the procedures introduced in Ref. [30] and used in EPOS2. Whereas the new procedure is very simple and clear concerning its definition, the numerical implementation turned out to be very difficult, owing to the fact that we use for many quantities prefabricated tables, making it possible to do fast interpolations during the Monte Carlo iterations (as a reminder: as explained in Ref. [3], we use Metropolis techniques to deal with the multidimensional phase space). However, only the new method gives a consistent picture and provides what is expected from common sense, like binary scaling at high p_t, which is not the case in the old method. The latter one is particularly unable (for whatever parameter choice) to reproduce experimental p-Pb results at the LHC, showing a nuclear modification factor (rescaled p-Pb/p-p) to be unity at large p_t, whereas the new method perfectly reproduced these data.

The saturation scale procedure is therefore a substantial improvement of our scheme, not only compatible with new theoretical developments during the past two decades [24–29], but also allowing a self-consistent treatment of soft and hard physics in a unique approach.

III. FLUX TUBES

Our master formula Eq. (1) makes it possible to compute total cross sections and (even more importantly) partial cross sections for particular multiple scattering configurations in p-p, p-A, and AA scatterings. The corresponding integrands can be interpreted as probability distributions of such configurations and serve as basis of Monte Carlo applications (see Ref. [3]). Here, contrary to many other Monte Carlo calculations, our events are real physical events; there is no need to introduce "test particles" and all kinds of fluctuations can be treated based on event-by-event fluctuations.

Generating an event is done in several steps.

(i) Step 1 amounts to generating the multiple scattering configuration according to Eq. (1), characterized by the number of cut Pomerons per possible nucleon-nucleon pair, and the light cone momentum fractions $x^{\pm}$ of the Pomeron ends. For example, for Au-Au or Pb-Pb collisions, with around 40 000 nucleon-nucleon pairs, one has up to 10^6 variables to generate, which requires sophisticated Monte Carlo methods [3].
(ii) Step 2 amounts to generate, for a given configuration, the partons associated to each Pomeron, based on the expressions representing a cut Pomeron, Eqs. (2)–(4). This time we are not using the integrals in these equations (needed in step 1), but their integrands, which serve as probability distributions.

The chain of partons corresponding to a given Pomeron is referred to as parton ladder. These ladders are identified with flux tubes, as explained in Ref. [3]. As a first step, for a given scattering, one considers the color flow. In Fig. 4, we show as an example two cut Pomerons of the "sea-sea" contribution, with a simple $gg \to gg$ elementary scattering, without initial- and final-state cascade. The projectile and target remnants stay always color neutral (they simply become excited). The actual interactions concern sea quarks, in the example of Fig. 4 the (anti)quarks q_1,$\bar{q}_1$ q_2,$\bar{q}_2$ for the first Pomeron, and q_3,$\bar{q}_3$ q_4,$\bar{q}_4$ for the second one. As a first step, one considers the color flow, shown in Fig. 4 by the red, blue, and green lines. Once the color flow is identified, one follows the line from a quark, via intermediate gluons, until an antiquark is found. In the example, we have $q_1 - g_1 - \bar{q}_2$ and $q_2 - g_2 - \bar{q}_1$ for the first Pomeron and $q_3 - g_3 - \bar{q}_4$ and $q_4 - g_4 - \bar{q}_3$ for the second

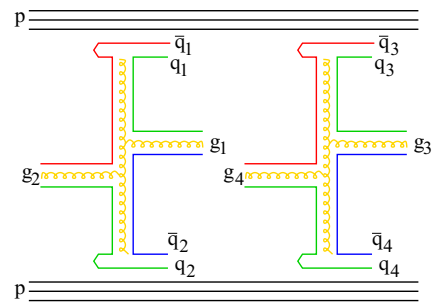

FIG. 4. (Color online) Color flow, for double Pomeron exchange, for a simplified scattering, without initial and final-state cascade.

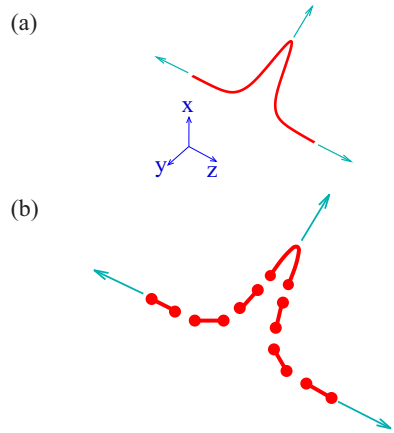

FIG. 5. (Color online) (a) Flux tube with transversely moving part (kinky string) in space, at given proper time. (b) Flux tube breaking via q-$\bar{q}$ production, which screens the color field (Schwinger mechanism).

one. Each of these four parton sequences is identified with a so-called "kinky string."

The relativistic string picture [31–33] is very attractive, because its dynamics is essentially derived from general principles as covariance and gauge invariance. The simplest possible string is a surface $X(\alpha,\beta)$ in $3+1$ dimensional space-time, with piecewise constant initial velocities $\partial X/\partial\beta$. These velocities are identified with parton velocities, which provides a one-to-one mapping from partons to strings. For details, see Refs. [3,4]. In the above example, we have four strings with a single kink each. The physical picture behind the "kinky string" is an essentially one-dimensional "color flux tube" (with eventually a finite but very small transverse dimension).

The high transverse momentum (p_t) partons will show up as transversely moving string pieces; see Fig. 5(a). Despite the fact that in the TeV energy range most processes are hard, and despite the theoretical importance of very high-p_t partons, it should not be forgotten that the latter processes are rare, most kinks carry only few GeV of transverse momentum, and the energy is nevertheless essentially longitudinal. In case of elementary reactions, the strings will break [see Fig. 5(b)] via the production of quark-antiquark pairs according to the so-called area law [3,4,34,35]. The string segments are identified with final hadrons and resonances.

This picture has been very successful to describe particle production in electron-positron annihilation or in proton-proton scattering at very high energies. In the latter case, not only are low-p_t particles described correctly, for example, for p-p scattering at 7 TeV [6,7], but jet production is also covered. As discussed earlier, the high transverse momenta of the hard partons show up as kinks, transversely moving string regions. After string breaking, the string pieces from these transversely moving areas represent the jets of particles associated with the hard partons. To demonstrate that this picture also works quantitatively, we compute the inclusive p_t distribution of jets, reconstructed with the anti-kt algorithm [36] and compare with data from ATLAS [37,38] and ALICE [39]; see Fig. 6.

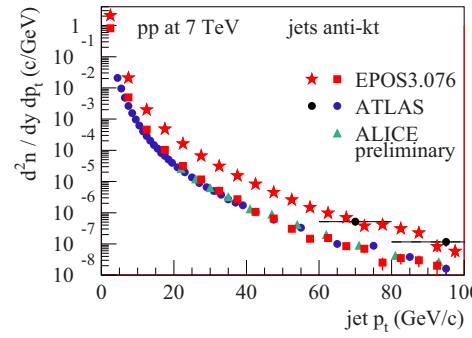

FIG. 6. (Color online) Inclusive p_t distribution of jets. We show the calculation (red stars) compared to ATLAS data [37] (black circles). We also show the calculated p_t distribution of charged particle jets (red squares) compared to data from ATLAS (blue circles) [38] and ALICE (green triangles) [39].

IV. CORE-CORONA PROCEDURE FOR PROTON-NUCLEUS SCATTERING

In HI collisions and also in high-multiplicity events in proton-proton and proton-nucleus scattering at very high energies, the density of strings will be so high that the strings cannot decay independently as described above. Here we have to modify the procedure as discussed in the following. The starting point is still the flux tubes (kinky strings) discussed earlier. Some of these flux tubes will constitute bulk matter, which thermalizes and expands collectively; this is the so-called "core." Other segments, being close to the surface or having a large transverse momentum, will leave the "bulk matter" and show up as hadrons (including jet hadrons); this is the so-called "corona."

In principle, the core-corona separation is a dynamical process. However, the knowledge of the initial transverse momenta p_t of string segments and their density $\rho(x,y)$ allows already an estimate about the fate of these string segments. By "initial" we mean some early proper time τ_0 which is a parameter of the model. In a first version of this "core-corona" approach [40], the core was simply defined by the string segment density (being bigger than some critical density ρ_0). More recently [5], we also considered the transverse momentum of the segments, to allow a high-p_t segment to leave the bulk part. This procedure was able to describe flow features and jet production at the same time.

Whereas our core-corona procedures (old and new ones) are always based on flux tubes (coming from Gribov-Regge multiple scattering), there are also core-corona models [41–44] based on the "wounded nucleon approach," where the core multiplicity is proportional to the number of participating nucleons having suffered at least two collisions, whereas the nucleons colliding only once contribute to the corona.

In our new core-corona procedure, for the moment optimized for p-p and p-A scattering, string segments constitute bulk matter or escape, depending on their transverse momenta p_t and the local string density ρ. We compute for each string segment

$$p_t^{\text{new}} = p_t - f_{\text{Eloss}} \int_\gamma \rho\, dL, \tag{11}$$

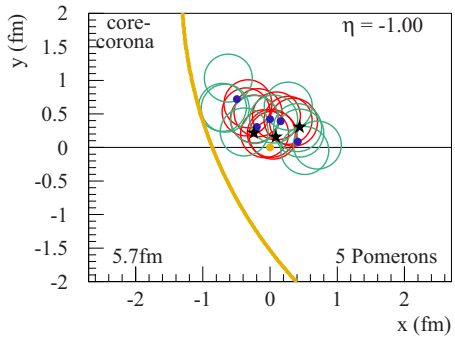

FIG. 7. (Color online) Core-corona separation in a randomly chosen p-Pb event (with an impact parameter of 5.7 fm) in the transverse plane at space-time rapidity $\eta_s = -1$. We show the positions of the projectile nucleon (yellow dot), the Pb surface (yellow line), the hit target nucleons (stars), the Pomerons (blue dots), as well as the core (red circles) and the corona (green circles) string segments.

where γ is the trajectory of the segment and f_{Eloss} is a nonzero constant for $p_t < p_{t,1}$, zero for $p_t > p_{t,2}$, and with a linear interpolation between $p_{t,1}$ and $p_{t,2}$. If a segment has a positive p_t^{new}, it is allowed to escape; it is a corona particle. Otherwise, the segment contributes to the core.

In Fig. 7, we show as an example the core-corona separation in a randomly chosen p-Pb event, by plotting the transverse plane at space-time rapidity $\eta_s = -1$. The yellow dot at $x = y = 0$ is the position of the projectile proton, the yellow line represents the target Pb surface (considering a hard sphere for the plot, whereas all calculations are done with a realistic Woods-Saxon distribution). The black stars mark the nucleons of the Pb nucleus, hit by the proton. The blue dots mark the transverse positions of the Pomerons; the flux tubes are scattered around these Pomeron points. Flux-tube segments contributing to the core are shown as red circles, the green ones represent the corona. The latter ones will show up as hadrons, whereas the core provides the initial condition of a hydrodynamical evolution (discussed in the next section), where the particles will be produced later at "freeze-out" from the flowing medium, which occurs at some "hadronization temperature" T_H [4]. After this "hadronization" the hadrons still interact among each other, realized via a hadronic cascade procedure [45], already discussed in Ref. [4].

In Fig. 8, we show how core and corona contribute to the production of pions and protons, for different centralities (based on impact parameter). The corona contributions dominate completely the high-p_t regions for all centralities. For central collisions (0%–5%), the core dominates for both pion and protons at low p_t, but the dominance (core over corona) is much more pronounced for protons, and the crossing (core = corona) happens at larger p_t (3.5 GeV/c) for the protons compared to pions (2–2.5 GeV/c). The fact that the core is much more visible in protons compared to pions is a consequence of radial flow: When particles are produced in a radially flowing medium, the heavier particles acquire more transverse momentum than the light ones. It is a mass effect (lambdas look similar to protons, kaons are between pions and protons). Going to more peripheral collisions, the flow effects

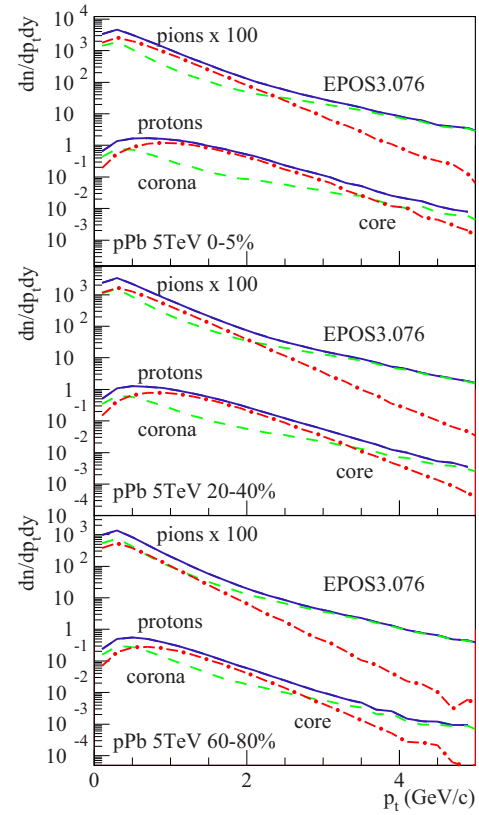

FIG. 8. (Color online) Core (red dash-dotted lines) and corona contributions (green dashed lines) to the production of pions (upper curves, multiplied by 100) and protons (lower curves), for different centralities in p-Pb collision at 5 TeV. The blue solid lines are the sum of core and corona. The calculations are done based on the hydrodynamical evolution as described in the next chapter, without employing a hadronic cascade.

get smaller, but even for peripheral events (60%–80%), we still have flow (actually even in p-p).

V. VISCOUS HYDRODYNAMICS

The core extracted as described above provides the initial condition for a hydrodynamic evolution. As explained in Ref. [4], we compute the energy-momentum tensor and the flavor flow vector at some position x (at $\tau = \tau_0$) from the four-momenta of the bulk string segments. The time $\tau = \tau_0$ is as well taken to be the initial time for the hydrodynamic evolution. This seems to be a drastic simplification, the justification being as follows. We imagine to have a purely longitudinal scenario (described by flux tubes) until some proper time $\tau_{\text{flux}} < \tau_0$. During this stage there is practically no transverse expansion, and the energy per unit of space-time rapidity does not change. This property should not change drastically beyond τ_{flux}, so we assume it will continue to hold during thermalization between τ_{flux} and τ_0. So although we cannot say anything about the precise mechanism that leads to thermalization, and therefore we cannot compute the real $T^{\mu\nu}$, we expect at least the elements T^{00} and T^{0i} to stay close

to the flux-tube values, and we can use the flux-tube results to compute the energy density, as explained in the following.

Based on the four-momenta of string segments, we compute the energy momentum tensor and the flavor flow vector at some position x (at $\tau = \tau_0$) as [4]

$$T^{\mu\nu}(x) = \sum_i \frac{\delta p_i^\mu \delta p_i^\nu}{\delta p_i^0} g(x - x_i), \tag{12}$$

$$N_q^\mu(x) = \sum_i \frac{\delta p_i^\mu}{\delta p_i^0} q_i \, g(x - x_i), \tag{13}$$

where $q \in u,d,s$ represents the net flavor content of the string segments, and

$$\delta p = \left\{ \frac{\partial X(\alpha,\beta)}{\partial \beta}\delta\alpha + \frac{\partial X(\alpha,\beta)}{\partial \alpha}\delta\beta \right\} \tag{14}$$

are the four-momenta of the segments. The function g is a Gaussian smoothing kernel with a transverse width $\sigma_\perp = 0.25$ fm. The Lorentz transformation into the comoving frame gives

$$\Lambda^\alpha{}_\mu \Lambda^\beta{}_\nu T^{\mu\nu} = T^{\mu\nu}_{\rm com}, \tag{15}$$

where we define the comoving frame such that the first column of $T_{\rm com}$ is of the form $(\varepsilon,0,0,0)^T$. This provides four equations for the energy density ε in the comoving frame and the flow velocity components v^i, which may be solved iteratively [4]. The flavor density is then calculated as

$$f_q = N_q u, \tag{16}$$

with u being the flow four-velocity.

For the hydrodynamic calculations, we construct the equation of state as

$$p = p_Q + \lambda\,(p_H - p_Q), \tag{17}$$

where p_H is the pressure of a resonance gas and p_Q the pressure of an ideal quark gluon plasma, including bag pressure. We use

$$\lambda = \exp(-z - 3z^2)\Theta(T - T_c) + \Theta(T_c - T), \tag{18}$$

with

$$z = x/(1 + x/0.77), \quad x = (T - T_c)/\delta, \tag{19}$$

using $\delta = 0.24\exp(-\mu_b^2/0.4^2)$. This λ provides an equation of state in agreement with recent lattice data [46]; see Fig. 9.

In the following, we describe the $3+1$D viscous hydrodynamic approach and the corresponding hydrodynamic component of the EPOS3 model, which we call VHLLE (viscous HLLE-based algorithm) [47]. For the hydrodynamic evolution we choose Milne coordinates (and its natural frame) for the t-z plane in space-time (z being the collision axis). The new coordinates are expressed in terms of Minkowski coordinates $\{t,x,y,z\}$ as $\tau = \sqrt{t^2 - z^2}$, $\eta = \frac{1}{2}\ln(t+z)/(t-z)$, while the definitions of x and y coordinates are unchanged. The

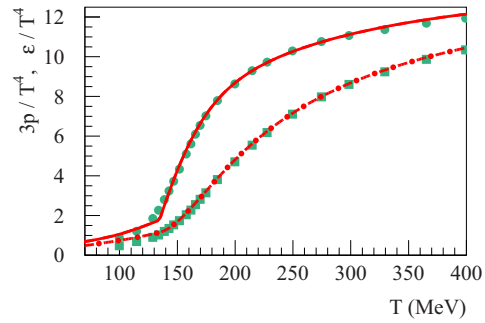

FIG. 9. (Color online) Energy density and pressure versus temperature for our equation-of-state (lines) compared to lattice data [46] (points).

transformation tensor M is

$$\left\{M^\mu_\nu\right\} = \begin{pmatrix} \cosh\eta & 0 & 0 & -\sinh\eta \\ 0 & 1 & 0 & 0 \\ 0 & 0 & 1 & 0 \\ -\frac{1}{\tau}\sinh\eta & 0 & 0 & \frac{1}{\tau}\cosh\eta \end{pmatrix}. \tag{20}$$

We choose $(+,-,-,-)$ signature of $g_{\mu\nu}$ in Minkowski space-time, so in Milne coordinates the invariant interval is $ds^2 = dt^2 - dx^2 - dy^2 - \tau^2 d\eta^2$ and the metric tensor is

$$g^{\mu\nu} = \mathrm{diag}(1,-1,-1,-1/\tau^2). \tag{21}$$

Although space-time is still flat, there are nontrivial Christoffel symbols, the nonzero components being

$$\Gamma^\eta_{\tau\eta} = \Gamma^\eta_{\eta\tau} = 1/\tau, \quad \Gamma^\tau_{\eta\eta} = \tau. \tag{22}$$

The hydrodynamic equations are given as

$$\partial_\nu T^{\mu\nu} = \partial_\nu T^{\mu\nu} + \Gamma^\mu_{\nu\lambda} T^{\nu\lambda} + \Gamma^\nu_{\nu\lambda} T^{\mu\lambda} = 0. \tag{23}$$

All source terms in Eq. (23) coming from $\Gamma^\nu_{\nu\lambda} T^{\mu\lambda}$ are proportional to $1/\tau$, which makes them dominant for the hydrodynamic evolution at small-enough τ and would eventually require to apply a higher-order numerical time integration scheme. We circumvent this by defining $\tilde{T}^{\mu\nu}$ via

$$\begin{aligned} T^{\mu\nu} &= \tilde{T}^{\mu\nu}, \quad \mu,\nu \neq \eta, \\ T^{\mu\eta} &= \tilde{T}^{\mu\eta}/\tau, \quad \mu \neq \eta, \\ T^{\eta\eta} &= \tilde{T}^{\eta\eta}/\tau^2, \end{aligned} \tag{24}$$

and we obtain from Eq. (23) equations for $\tau\tilde{T}^{\mu\nu}$,

$$\begin{aligned} &\tilde{\partial}_\nu(\tau\tilde{T}^{\tau\nu}) + \frac{1}{\tau}(\tau\tilde{T}^{\eta\eta}) = 0, \quad \tilde{\partial}_\nu(\tau\tilde{T}^{x\nu}) = 0, \\ &\tilde{\partial}_\nu(\tau\tilde{T}^{y\nu}) = 0, \quad \tilde{\partial}_\nu(\tau\tilde{T}^{\eta\nu}) + \frac{1}{\tau}\tau\tilde{T}^{\eta\tau} = 0, \end{aligned} \tag{25}$$

with

$$\tilde{\partial} \equiv [\partial/\partial\tau, \partial/\partial x, \partial/\partial y, (1/\tau)\partial/\partial\eta], \tag{26}$$

and thus all the $\tilde{T}^{\mu\nu}$ have the same units, as well as $\tilde{\partial}_\mu$, namely, [1/length]. The actual conservative variables used in the code are therefore $Q^\mu = \tau \cdot \tilde{T}^{\mu\tau}$; fluxes are $\tau \cdot \tilde{T}^{ij}$. Then Eqs. (25) are the explicit form of energy-momentum conservation equations which are solved numerically.

The energy-momentum tensor can be expanded in the case of a viscous fluid as

$$T^{\mu\nu} = \epsilon u^\mu u^\nu - (p+\Pi)\Delta^{\mu\nu} + \pi^{\mu\nu}, \tag{27}$$

where $\Delta^{\mu\nu} = g^{\mu\nu} - u^\mu u^\nu$ is the projector orthogonal to u^μ (u^μ being the flow field), and finally $\pi^{\mu\nu}$ and Π are the shear stress tensor and bulk pressure, respectively. Expressing the four-velocities $u_{\rm MS}$ in Minkowski space-time in terms of the longitudinal/transverse rapidities as

$$u_{\rm MS} = (\cosh\eta_f \cosh\eta_T,\ \sinh\eta_T\cos\phi,\ \sinh\eta_T\sin\phi,\ \sinh\eta_f\cosh\eta_T), \tag{28}$$

we get in Milne coordinates $u^\mu = M^\mu_\nu u^\nu_{\rm MS}$, which gives

$$u = [\cosh(\eta_f-\eta)\cosh\eta_T,\ \sinh\eta_T\cos\phi,\ \sinh\eta_T\sin\phi,\ \tau^{-1}\sinh(\eta_f-\eta)\cosh\eta_T]. \tag{29}$$

Defining $\tilde u = (u^\tau, u^x, u^y, \tau u^\eta)$, we have $\tilde T^{\eta\eta} = (\epsilon + p + \Pi)\tilde u^\eta \tilde u^\eta + (p+\Pi) + \pi^{\eta\eta}$, so both $\tilde u$ and $\tilde T^{\eta\eta}$ do not include the factor $1/\tau$ any more.

The hydrodynamic code used solves the equations of relativistic viscous hydrodynamics in Israel-Stewart framework [48]. In particular, we solve the following equations for the shear stress tensor and bulk pressure, neglecting vorticity terms:

$$\langle u^\gamma \partial_{;\gamma}\pi^{\mu\nu}\rangle = -\frac{\pi^{\mu\nu} - \pi^{\mu\nu}_{\rm NS}}{\tau_\pi} - \frac{4}{3}\pi^{\mu\nu}\partial_{;\gamma}u^\gamma, \tag{30}$$

$$u^\gamma \partial_{;\gamma}\Pi = -\frac{\Pi - \Pi_{\rm NS}}{\tau_\Pi} - \frac{4}{3}\Pi\partial_{;\gamma}u^\gamma, \tag{31}$$

where

$$\langle A^{\mu\nu}\rangle = \left(\tfrac{1}{2}\Delta^\mu_\alpha\Delta^\nu_\beta + \tfrac{1}{2}\Delta^\nu_\alpha\Delta^\mu_\beta - \tfrac{1}{3}\Delta^{\mu\nu}\Delta_{\alpha\beta}\right)A^{\alpha\beta}$$

denotes the symmetric and traceless part of $A^{\mu\nu}$ being orthogonal to u^μ, and

$$\pi^{\mu\nu}_{\rm NS} = \eta(\Delta^{\mu\lambda}\partial_{;\lambda}u^\nu + \Delta\nu\lambda\partial_{;\lambda}u^\mu) - \tfrac{2}{3}\eta\Delta^{\mu\nu}\partial_{;\lambda}u^\lambda,$$
$$\Pi_{\rm NS} = -\zeta\,\partial_{;\lambda}u^\lambda, \tag{32}$$

are the values of the shear stress tensor and bulk pressure in the limiting Navier-Stokes case.

For the purpose of our current study, we do not include the baryon/electric charge diffusion. The same choice for the evolutionary equations (30) was used in the recent studies of p-A collisions employing relativistic viscous hydrodynamics [8,9].

In the same way as was done for $T^{\mu\nu}$, we separate the factors $1/\tau$ from $\pi^{\mu\nu}$ by defining $\tilde\pi^{\mu\nu}$ as follows:

$$\pi^{\mu\nu} = \tilde\pi^{\mu\nu}, \quad \mu,\nu \neq \eta,$$
$$\pi^{\mu\eta} = \tilde\pi^{\mu\eta}/\tau, \quad \mu \neq \eta, \tag{33}$$
$$\pi^{\eta\eta} = \tilde\pi^{\eta\eta}/\tau^2.$$

We rewrite Eqs. (30) and (31) in the form used for the numerical solution,

$$\tilde\gamma(\partial_\tau + \tilde v^i\tilde\partial_i)\tilde\pi^{\mu\nu} = -\frac{\tilde\pi^{\mu\nu} - \tilde\pi^{\mu\nu}_{\rm NS}}{\tau_\pi} + I^{\mu\nu}_\pi, \tag{34}$$

$$\tilde\gamma(\partial_\tau + \tilde v^i\tilde\partial_i)\Pi = -\frac{\Pi - \Pi_{\rm NS}}{\tau_\Pi} + I_\Pi, \tag{35}$$

where $\tilde\gamma = u^0$ and $\tilde v^i = \tilde u^i/u^0$ ($i = x,y,\eta$) are the components of 3-velocity. The additional source terms are

$$I^{\mu\nu}_\pi = -\tfrac{4}{3}\tilde\pi^{\mu\nu}\tilde\partial_{;\gamma}\tilde u^\gamma - [\tilde u^\nu\tilde\pi^{\mu\beta} + \tilde u^\mu\tilde\pi^{\nu\beta}]\tilde u^\lambda\tilde\partial_{;\lambda}\tilde u_\beta - I^{\mu\nu}_{\pi,G}, \tag{36}$$

$$I_\Pi = -\tfrac{4}{3}\Pi\tilde\partial_{;\gamma}\tilde u^\gamma, \tag{37}$$

with $\tilde\partial_{;\gamma}\tilde u^\gamma = \tilde\partial_\gamma\tilde u^\gamma + u^\tau/\tau$. The terms $I^{\mu\nu}_{\pi,G}$ denote geometrical source terms (coming from Christoffel symbols), given as

$$I^{\tau\tau}_{\pi,G} = 2\tilde u^\eta\tilde\pi^{\tau\eta}/\tau, \quad I^{\tau x}_{\pi,G} = \tilde u^\eta\tilde\pi^{\eta x}/\tau,$$
$$I^{\tau y}_{\pi,G} = \tilde u^\eta\tilde\pi^{\eta y}/\tau, \quad I^{\tau\eta}_{\pi,G} = \tilde u^\eta(\tilde\pi^{\tau\tau} + \tilde\pi^{\eta\eta})/\tau,$$
$$I^{\eta x}_{\pi,G} = \tilde u^\eta\tilde\pi^{\tau x}/\tau, \quad I^{\eta y}_{\pi,G} = \tilde u^\eta\tilde\pi^{\tau y}/\tau,$$
$$I^{\eta\eta}_{\pi,G} = 2\tilde u^\eta\tilde\pi^{\tau\eta}/\tau, \quad I^{xx}_{\pi,G} = I^{xy}_{\pi,G} = I^{xy}_{\pi,G} = 0.$$

To solve the energy-momentum conservation equations (25) in the viscous case, we use the technique of ideal-viscous splitting [49]. This allows us to solve the ideal part very accurately using Godunov method, employing relativistic HLLE approximation for the solution of Riemann problem. Israel-Stewart equations (30) and (31) are solved in parallel, and then the evolution of energy/momentum is corrected according to viscous fluxes and source terms in Eq. (25).

VI. TESTING THE HYDRO PROCEDURE

For the purpose of current paper we skip presenting technical details of the code and the results of basic tests against analytical hydro solutions, leaving that to a separate publication. However, in what follows, we compare our hydro simulations to the results of "open TECHQM" [50], using the same initial conditions for HI collisions as they propose, namely,

$$\begin{aligned}\epsilon(\tau_0,r_x,r_y) &= C\cdot n_{WN}(r_x,r_y)\\ &= CT_A(r_x+b/2,r_y)\\ &\quad\times\{1-[1-T_A(r_x-b/2,r_y)\sigma_{NN}/A]^A\}\\ &\quad + CT_A(r_x-b/2,r_y)\\ &\quad\times\{1-[1-T_A(r_x+b/2,r_y)\sigma_{NN}/A]^A\},\end{aligned} \tag{38}$$

where the nuclear thickness function $T_A(x,y) = \int dr_z\rho(r_x,r_y,r_z)$ is normalized such that $\int T_A(x,y)dxdy = A$, and $\rho(r_x,r_y,r_z) = c/\{\exp[(r-R_A)/\delta]+1\}$ is the density distribution for nucleons in the nucleus. For Au-Au collision the parameters are $A = 197$, $R_A = 6.37$ fm, $\delta = 0.54$ fm, $\sigma_{NN} = 40$ mb is the inelastic nucleon-nucleon cross section and C is chosen so that $\epsilon_0(0,0;b=0) = 30$ GeV/fm^3. The equation of state (EoS) for relativistic massless gas $p = \epsilon/3$ is used. To extract the temperature in this EoS, we assume 2.5 massless quark degrees of freedom and $g_q = 2\times2\times3 = 12$ degeneracy factor and $g_g = 16$ for massless gluons. For viscous hydro runs we fix bulk viscosity to zero and initialize $\pi^{\mu\nu}$ at τ_0 with their Navier-Stokes values, which yields $\pi^{xx} = \pi^{yy} = -\tau^2\pi^{\eta\eta}/2 = 2\eta/(3\tau_0)$.

In Fig. 10 we show the comparison for average transverse velocity as a function of evolution time τ for initial conditions

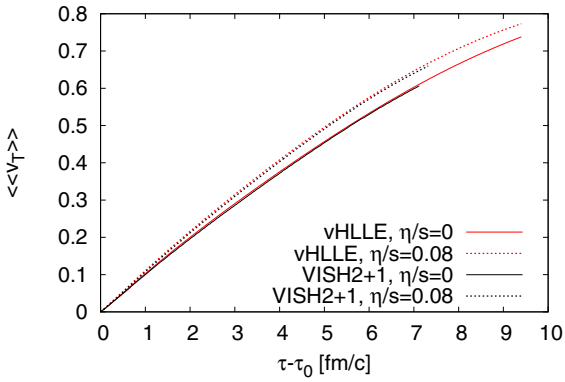

FIG. 10. (Color online) Averaged radial flow as a function of proper time for our hydro code (VHLLE) compared to VISH2+1 by H. Song

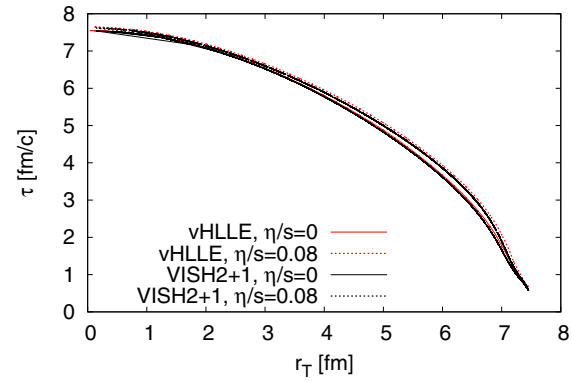

FIG. 12. (Color online) Isothermal surface corresponding to $T_f = 130$ MeV obtained with our hydro code (VHLLE) compared to the results from VISH2+1 by H. Song

with impact parameter $b = 0$. The average is defined as

$$\langle\langle v_T \rangle\rangle = \int \frac{v_T \cdot \epsilon}{\sqrt{1 - v_T^2}} d^2 r_T,$$

with $v_T = \sqrt{v_x^2 + v_y^2}$, and where the integration is made for a slice of system (cells) with rapidity $y = 0$. Shear viscosity works to equalize the expansion in different directions, thus decelerating the initially strong longitudinal expansion and accelerating transverse one, which results in additional acceleration of transverse radial flow. One can see that the magnitude of the effect in our results is consistent with those from VISH2+1 code.

In the same way, shear viscosity suppresses the development of flow anisotropy in the transverse plane, the latter being generated by anisotropic pressure gradients in hydrodynamics. To check this effect, we set the initial conditions for $b = 7$ fm and in Fig. 11 we show the corresponding time evolution of flow anisotropy, defined as

$$\epsilon_p = \frac{\langle T_{\rm id}^{xx} - T_{\rm id}^{yy} \rangle}{\langle T_{\rm id}^{xx} + T_{\rm id}^{yy} \rangle}, \quad \epsilon_p' = \frac{\langle T^{xx} - T^{yy} \rangle}{\langle T^{xx} + T^{yy} \rangle}, \tag{39}$$

with $\langle \cdots \rangle = \int \cdots d^2 r_T$; the quantities ϵ_p and ϵ_p' are calculated using the ideal part of the energy-momentum tensor and full energy-momentum tensor, respectively. The suppression of ϵ_p comes solely from the rearrangement of collective flow, while ϵ_p' is suppressed stronger owing to contributions from $\pi^{\mu\nu}$. The results are as well consistent with the ones from the VISH2+1 code.

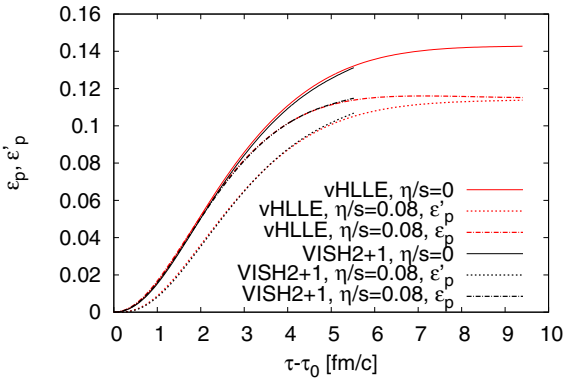

FIG. 11. (Color online) Flow anisotropies ϵ_p and ϵ_p' (see text for explanation) as a function of proper time for our hydro code (VHLLE) compared to VISH2+1 by H. Song

Finally, in Fig. 12, we show the isothermal surfaces for the case $b = 0$ corresponding to temperature $T_f = 130$ MeV (or $\epsilon_f = 0.516\,\text{GeV/fm}^3$). Here slight differences may come from the details (interpolation scheme) to determine the position of freeze-out surface, so the discrepancies less than $\Delta x/2 = 0.1$ fm are justified.

VII. PARAMETERS AND BASIC TESTS

Our basic framework for the initial conditions is "parton-based Gribov-Regge theory," described in detail in Ref. [3]. In that paper we dedicate a whole section to the discussion of parameters that is still valid now. All "basic" parameters (see Table 8.2 in Ref. [3]) related to define the multiple scattering amplitude discussed earlier are fixed by comparing to proton-proton data.

There are very few parameters related to the "new features" discussed earlier. There are first of all the two coefficients $A_{\rm sat}$ and $B_{\rm sat}$ in the saturation scale formulas: They are used to assure binary scaling in p-A and AA scattering at large p_t and a correct energy dependence of the total cross section in p-p. It should be said that the former "screening" procedure introduced in Ref. [30] had at the end more than 20 parameters, without satisfying results in p-A scattering. The new method (with two parameters) gives a much more consistent picture for p-p and p-A at LHC energies. Also, Pb-Pb results look promising, but in this paper we concentrate on p-A.

The new core-corona procedure depends on the coefficient $f_{\rm Eloss}$, which is the most important parameter for the analysis presented in this paper: Increasing this constant will increase the core contribution. Putting $f_{\rm Eloss} = 0$ would completely suppress the core; we have a pure string model. Making $f_{\rm Eloss}$ very big leads to a purely hydrodynamic expansion. The reality seems to be between these two extremes: All the results shown in this paper refer to $f_{\rm Eloss} = 0.137\,\text{fm GeV}/c$.

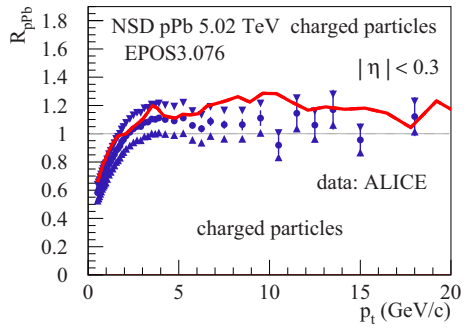

FIG. 13. (Color online) The nuclear modification factor for non single diffractive (NSD) p-Pb scattering at 5.02 TeV. We show our full calculation, EPOS3 with hydro and hadronic cascade (solid red line), compared to data from ALICE [54] (error bars refer to statistical errors, triangles to systematic errors).

Finally, we use in our approach for the first time viscous hydrodynamics for the collective expansion. All calculations shown are done for shear viscosity over entropy density (η/s) of 0.08. We fix bulk viscosity to zero, and we do not include the baryon/electric/strange charge diffusion either. Furthermore, we initialize $\pi^{\mu\nu}$ at τ_0 with their Navier-Stokes values, which yields $\pi^{xx} = \pi^{yy} = -\tau^2\pi^{\eta\eta}/2 = 2\eta/(3\tau_0)$, and the relaxation time for the shear stress tensor is taken as $\tau_\pi = 3\eta/(sT)$.

Before analyzing in detail identified-particle spectra, we first show in Figs. 13–15 some basic tests of our approach. In Fig. 13, we compare our calculations to the experimental nuclear modification factor $R_{p\mathrm{Pb}}$ (rescaled p-Pb spectra over p-p). Beyond 2–3 GeV/c, both curves are compatible with unity.

In Fig. 14, we show p_t spectra of charged particles for NSD p-Pb scattering at 5.02 TeV, for three different

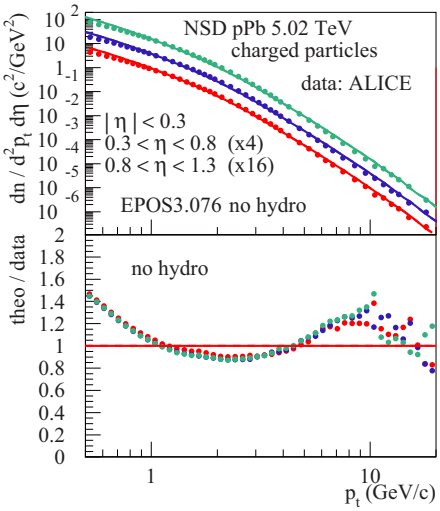

FIG. 14. (Color online) Transverse momentum spectra of charged particles for NSD p-Pb scattering at 5.02 TeV for three different pseudorapidity windows. We show data from ALICE [54], compared to our "basic" calculation without hydro, without cascade, as well as the ratio theory over data.

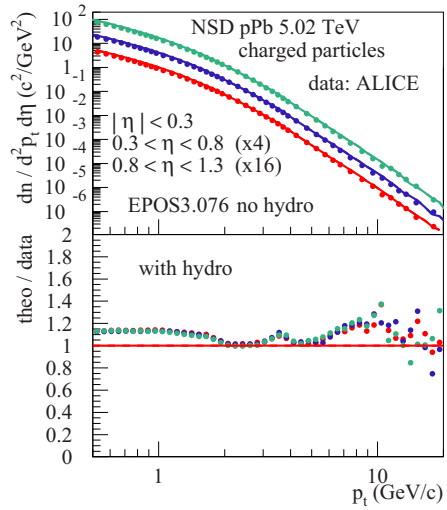

FIG. 15. (Color online) Same as Fig. 14, but showing the full calculation, with hydro and hadronic cascade.

pseudorapidity windows. We compare our calculation without hydro to experimental ALICE data. The simulation results are significantly below the data in the p_t range of 1 to 5 GeV/c. There is nothing one can do (via parameter change) to significantly improve the agreement without hydro. In Fig. 15, we compare the same experimental data to our full calculation, with hydro and hadronic cascade. Taking into account the hydro evolution improves the situation considerably.

VIII. HADRONIZATION

The system hadronizes in the cross-over region, where here "hadronization" is meant to be the end of the completely thermal phase: Matter is transformed into hadrons. We stop the hydrodynamical evolution at this point, but particles are not yet free. Our favorite hadronization temperature T_H is 168 MeV, which is indeed right in the transition region, where the energy density varies strongly with temperature. At this point we employ statistical hadronization, which should be understood as hadronization of the quark-gluon plasma state into a hadronic system, at an early stage, not the decay of a resonance gas in equilibrium. To be more precise, we employ the Cooper-Frye prescription on a hypersurface defined by constant T_H. The hadronization procedure is described in detail in the appendix of Ref. [4].

After this hadronization—although no longer thermal—the system still interacts via hadronic scatterings, still building up (elliptical) flow, but much less compared to an idealized thermal resonance gas evolution, which does not exist in reality. The particles at their hadronization positions (on the corresponding hypersurface) are fed into the hadronic cascade model URQMD [45], performing hadronic interactions until the system is so dilute that no interaction occurs any more. The "final" freeze-out position of the particles is the last interaction point of the cascade process, or the hydro hadronization position, if no hadronic interactions occurs.

IX. IDENTIFIED-PARTICLE RESULTS FOR p-Pb

In the following, we compare experimental data on identified particle production with our simulation results (referred to as EPOS3), and in addition to some other models, as there are QGSJETII [51], AMPT [52], and EPOS LHC [53]. The QGSJETII model is also based on Gribov-Regge multiple scattering, but there is no fluid component. The main ingredients of the AMPT model are a partonic cascade and then a hadronic cascade, providing in this way some "collectivity." EPOS LHC is a tune (using LHC data) of EPOS1.99. As all EPOS1 models, it contains flow, put in by hand, parametrizing the collective flow at freeze-out. Finally, the approach discussed in this paper (EPOS3) contains a full viscous hydrodynamical simulation. So it is interesting to compare these four models, because they differ considerably concerning the implementation of flow, from full hydrodynamical flow in EPOS3 to no flow in QGSJETII.

The CMS collaboration published a detailed study [1] of the multiplicity dependence of (normalized) transverse momentum spectra in p-Pb scattering at 5.02 TeV. The multiplicity (referred to as N_{track}) counts the number of charged particles in the range $|\eta| < 2.4$. Many multiplicity classes have been considered, but in our analysis we consider only four, so as not to overload the figures. The mean values of the four multiplicity classes are 8, 84, 160, and 235.

In Fig. 16, we compare experimental data [1] for pions (black symbols) with the simulations from QGSJETII (top left panel), AMPT (top right), EPOS LHC (bottom left), and EPOS3 (bottom right). The different curves in each figure refer to different centralities, with mean values (from bottom to top) of 8, 84, 160, and 235 charged tracks. They are shifted relative to each other by a constant amount. Concerning the models, QGSJETII is the easiest to discuss, because here there are no flow features at all, and the curves for the different multiplicities are identical. The data, however, show a slight centrality

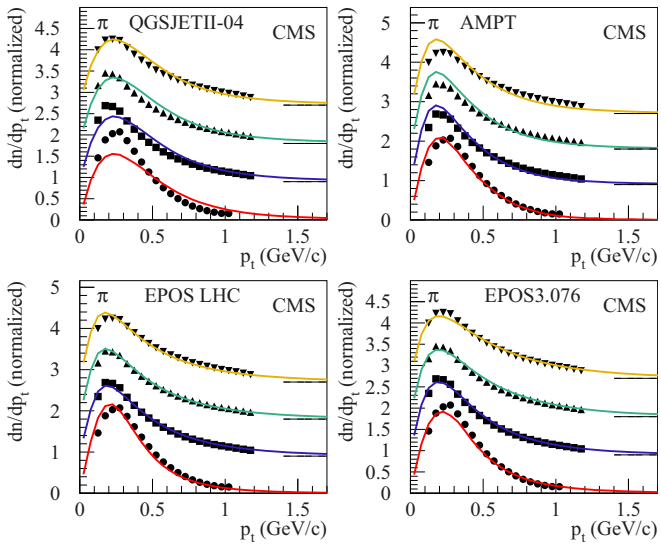

FIG. 16. (Color online) Transverse momentum spectra of pions in p-Pb scattering at 5.02 TeV for four different multiplicity classes with mean values (from bottom to top) of 8, 84, 160, and 235 charged tracks. We show data from CMS [1] (symbols) and simulations from QGSJETII, AMPT, EPOS LHC, and EPOS3, as indicated in the figures.

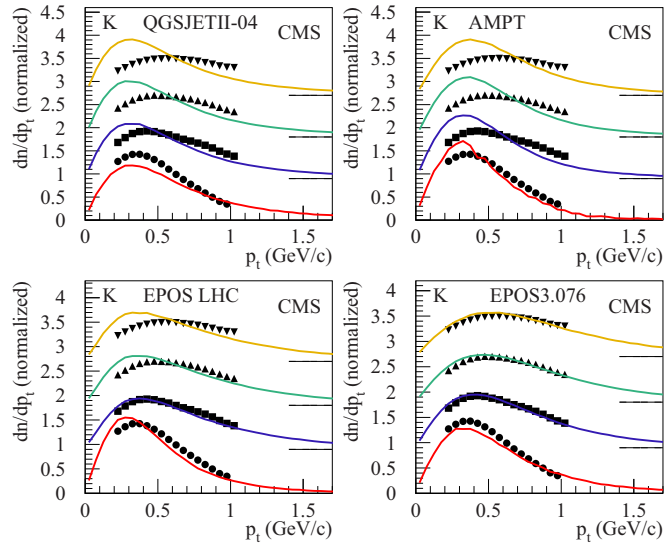

FIG. 17. (Color online) Same as Fig. 16, but for kaons.

dependence: The spectra get somewhat harder with increasing multiplicity. The other models, AMPT, EPOS LHC, and EPOS3, are close to the data.

In Fig. 17, we compare experimental data [1] for kaons (black symbols) with the simulations. In the data, the shapes of the p_t spectra change considerably with multiplicity: They get much harder with increasing multiplicity. In QGSJETII, there is again no change and in AMPT too little change with multiplicity. EPOS LHC goes into the right direction, whereas EPOS3 gives a satisfactory description of the data. In Fig. 18, we compare experimental data [1] for protons (black symbols) with the simulations. Again, as for kaons, the experimental shapes of the p_t spectra change considerably, getting much harder with increasing multiplicity. In QGSJETII, having no flow, the curves for the different multiplicities are identical. The AMPT model shows some (but too little) change with multiplicity. EPOS LHC goes into the right direction, whereas EPOS3 gives a reasonable

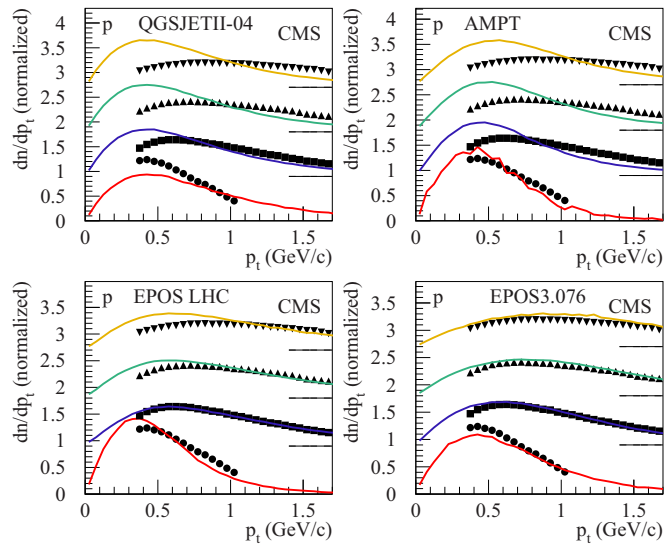

FIG. 18. (Color online) Same as Fig. 16, but for protons.

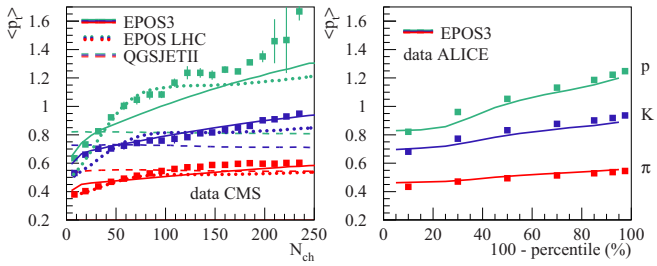

FIG. 19. (Color online) Multiplicity dependence of the average transverse momentum of protons (green), kaons (blue), and pions (red) in p-Pb scattering at 5.02 TeV. (Left) Data from CMS [1] (symbols) and simulations from QGSJETII (dashed lines), EPOS LHC (dotted lines), and EPOS3 (solid lines). (Right) Data from ALICE and EPOS3 results (percentiles are defined via the VZERO-A multiplicity).

description of the data. *It seems that hydrodynamical flow helps considerably to reproduce these data.*

Based on these multiplicity-dependent p_t spectra, one obtains the multiplicity dependence of the average transverse momentum $\langle p_t \rangle$, as shown in Fig. 19 (left), where we plot the multiplicity dependence of the average transverse momentum of protons (green), kaons (blue), and pions (red) in p-Pb scattering at 5.02 TeV. We show data from CMS [1] (symbols) and simulations from QGSJETII (dashed lines), EPOS LHC (dotted lines), and EPOS3 (solid lines). Whereas QGSJETII shows no multiplicity dependence, EPOS LHC and EPOS3 increase with multiplicity, and this increase is more pronounced for heavier particles (owing to the radial flow). However, EPOS LHC reaches a kind of plateau at high multiplicity, whereas data (and EPOS3) increase continuously. This is (in EPOS3) a core-corona effect: The core (=flow) fraction increases with multiplicity. In Fig. 19 (right), we compare $\langle p_t \rangle$ results from EPOS3 with data from ALICE [2], where we use "percentiles" defined via the VZERO-A multiplicity, as in the experiment. Again we see (in the data and the simulations) the same trend of increasing $\langle p_t \rangle$, more pronounced for heavier particles (a more detailed analysis of ALICE data will be given below).

All the discussions above are based on normalized (to unity) p_t spectra. To verify the absolute normalizations of the various particle yields, we plot in Fig. 20 $dn/dp_t dy$ (particles per event) for protons (green), kaons (blue), and pions (red) as a function of p_t, in p-Pb scattering at 5.02 TeV. We show data from CMS [1] (symbols) and simulations from QGSJETII (dashed lines), EPOS LHC (dotted lines), and EPOS3 (solid lines). The left panel shows the spectra; the right one shows the corresponding ratio theory over experiment. EPOS LHC and EPOS3 are compatible with the data, whereas QGSJETII seriously overpredicts baryon production at low transverse momentum.

Also, ALICE has measured identified-particle spectra for different multiplicities in p-Pb scattering at 5.02 TeV. The multiplicity counts the number of charged particles in the range $2.8 < \eta_{\rm lab} < 5.1$. Many classes have been considered; in this work, we consider the high-multiplicity (0%–5%) and the low-multiplicity (60%–80%) classes.

In Fig. 21, we show transverse momentum spectra of charged pions and kaons in p-Pb scattering at 5.02 TeV, for the 0%–5% and 60%–80% highest multiplicity event classes,

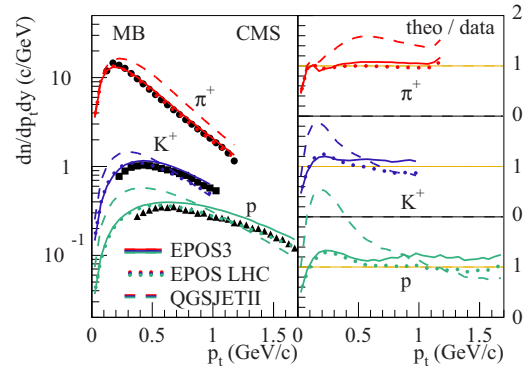

FIG. 20. (Color online) Transverse momentum spectra $dn/dp_t dy$ of protons (green), kaons (blue), and pions (red) in p-Pb scattering at 5.02 TeV. We show data from CMS [1] (symbols) and simulations from QGSJETII (dashed lines), EPOS LHC (dotted lines), and EPOS3 (solid lines). The left panel shows the spectra; the right one shows the corresponding ratio theory over experiment.

referred to as "high-multiplicity" and "low-multiplicity" events. We show data from ALICE [2] (symbols) and simulations from QGSJETII (dashed lines), AMPT (dashed-dotted), EPOS LHC (dotted), and EPOS3 (solid). In Fig. 22, we show the corresponding results for protons, neutral kaons, and lambdas. We show always the spectra for data and theory (left) as well

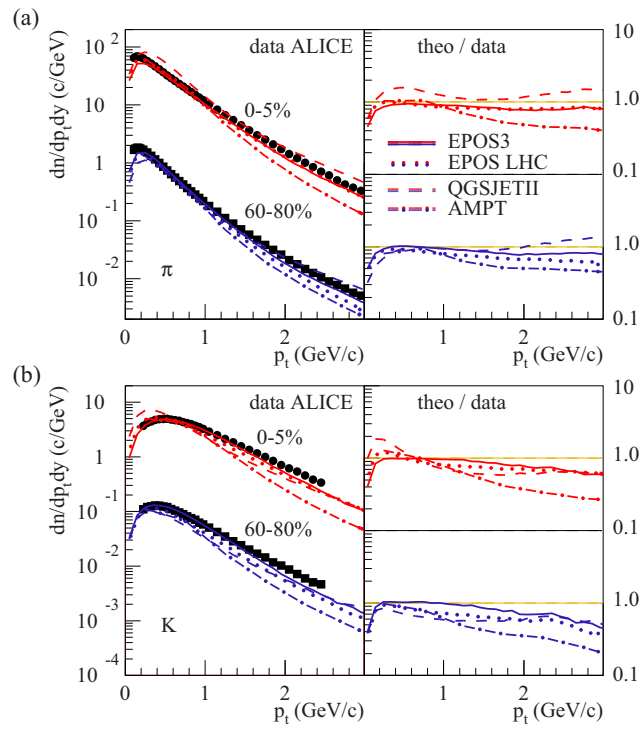

FIG. 21. (Color online) (a) Transverse momentum spectra of charged pions in p-Pb scattering at 5.02 TeV for two different multiplicity classes: 0%–5% highest multiplicity (red, upper plots) and low-multiplicity events, 60%–80% (blue, lower plots). We show data from ALICE [2] (symbols) and simulations from QGSJETII (dashed lines), AMPT (dash-dotted), EPOS LHC (dotted), and EPOS3 (solid). (b) Same as (a), but for charged kaons.

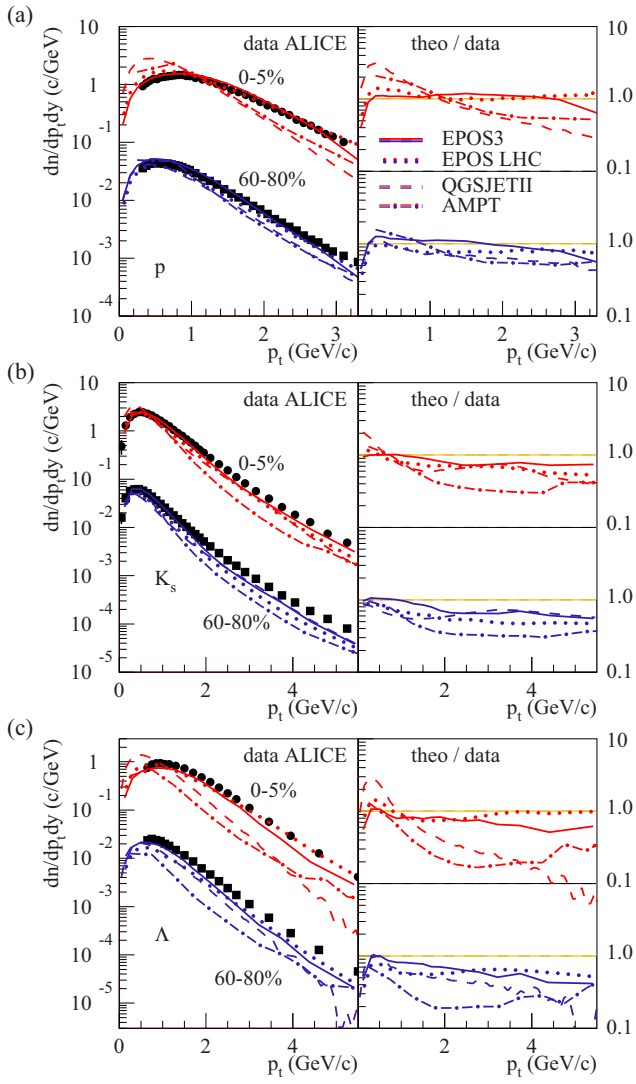

FIG. 22. (Color online) Same as Fig. 21, but for protons (a), neutral kaons (K_s) (b), and lambdas (c).

as the ratios theory over data (right). For the latter ones, we use logarithmic scales (with a range 0.1 to 10), because in some cases the models are off (compared to data) by more than a factor of 10.

In Ref. [2], the authors discuss in detail the multiplicity dependence, in particular by investigating particle ratios for high-multiplicity and low-multiplicity events. However, what is clear from Figs. 21 and 22 is that the models without flow or with little flow (QGSJETII, AMPT) considerably underpredict the intermediate p_t range, in particular for the baryons (protons and lambdas), for both high-multiplicity and low-multiplicity events. It is again the "flow effect" in EPOS LHC and EPOS3 which helps, pushing heavier particles to higher p_t values (in the range 2–4 GeV/c). It should be noted that even for the low-multiplicity events, flow is needed. As we have shown in Fig. 8 for EPOS3, even for "peripheral events" (60%–80%) the core (=flow) already contributes.

Flow seems to be always present for all multiplicities (or centralities), just the relative importance of the core part (and

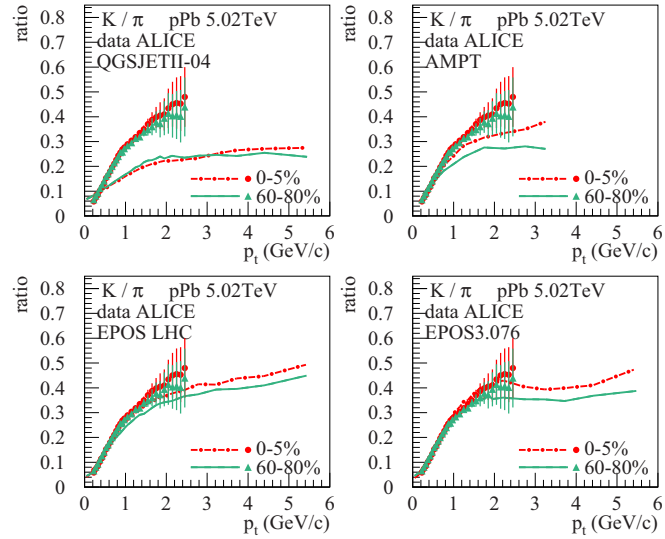

FIG. 23. (Color online) Kaon-over-pion ratio as a function of transverse momentum in p-Pb scattering at 5.02 TeV for two different multiplicity classes: 0%–5% highest multiplicity (red dash-dotted lines, circles) and low-multiplicity events, 60%–80% (green solid lines, triangles). We show data from ALICE [2] (symbols) and simulations from QGSJETII, AMPT, EPOS LHC, EPOS3 (lines).

therefore the flow) increases (moderately) with multiplicity. This leads immediately to the question of collective flow in proton-proton scattering, which we address later.

Nevertheless, it is useful to study the multiplicity dependence, best done by looking at ratios. In Fig. 23, we show the pion-over-kaon (K/π) ratio as a function of transverse momentum in p-Pb scattering at 5.02 TeV, for high-multiplicity (red dash-dotted lines, circles) and low-multiplicity events (green solid lines, triangles), comparing data from ALICE [2] (symbols) and simulations from QGSJETII, AMPT, EPOS LHC, and EPOS3 (lines). In all models, as in the data, there is little multiplicity dependence. However, the QGSJETII model is considerably below the data, for both high- and low-multiplicity events. AMPT is slightly below, whereas EPOS LHC and EPOS3 do a reasonable job. Concerning the proton-over-pion (p/π) ratio, Fig. 24, again QGSJETII is way below the data, for both high- and low-multiplicity events, whereas the three other models show the trend correctly, but being slightly above the data. Most interesting are the lambdas-over-kaon (Λ/K_s) ratios, as shown in Fig. 25, because here a wider transverse momentum range is considered, showing a clear peak structure with a maximum around 2–3 GeV/c and a slightly more pronounced peak for the higher multiplicities. QGSJETII and AMPT cannot (even qualitatively) reproduce this structure. EPOS LHC shows the right trend, but the peak is much too high for the high multiplicities. EPOS3 is close to the data.

To summarize these ratio plots (keeping in mind that the QGSJETII model has no flow, AMPT "some" flow, EPOS LHC a parametrized flow, and EPOS3 hydrodynamic flow): Flow seems to help considerably. However, from the Λ/K_s ratios, we conclude that EPOS LHC uses a too-strong radial flow for high-multiplicity events. The hydrodynamic flow employed in EPOS3 seems to get the experimental features reasonably well.

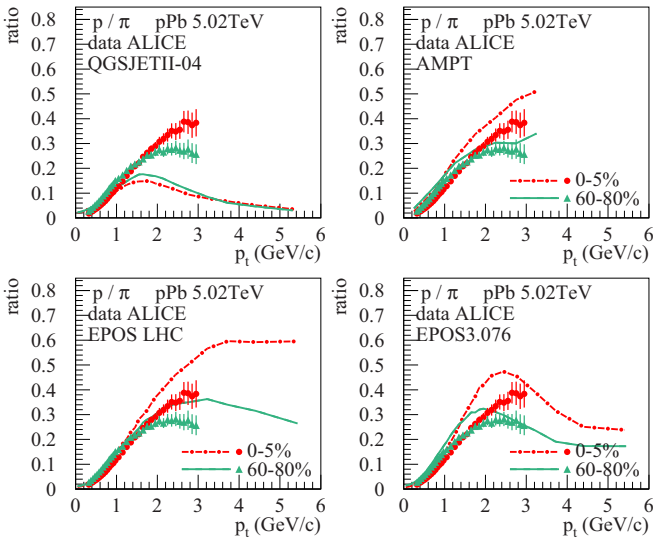

FIG. 24. (Color online) Same as Fig. 23, but proton-over-pion ratio.

Crucial is the core-corona procedure discussed earlier: There is more core (compared to corona) in more central collisions, but the centrality (or multiplicity) dependence is not so strong, and there is already an important core (=flow) contribution in peripheral events.

X. PROTON-PROTON SCATTERING AT 7 TeV

From our above studies of p-Pb scattering at 5.02 TeV, we conclude that hydrodynamical flow seems to play an important role, similar to that in HI collisions, contrary to all expectations. Even more surprisingly, these hydrodynamical features already appear in peripheral (or low-multiplicity) p-Pb events, being close to proton-proton scatterings. So after being obliged to give up the common prejudice that proton-nucleus scattering is a simple "baseline" compared to the hydrodynamically evolving HI collisions, do we have to do so for proton-proton scattering as well?

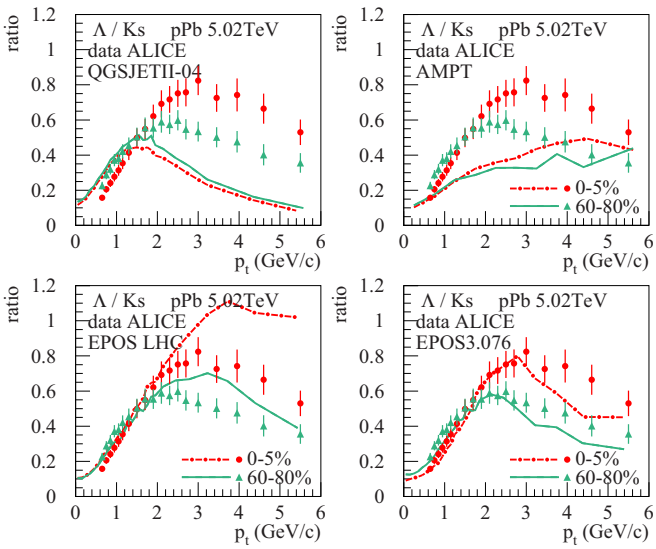

FIG. 25. (Color online) Same as Fig. 23, but Λ-over-K_s ratio.

TABLE I. List of models used to analyze identified-particle production in proton-proton scattering at 7 TeV. "GR" stands for Gribov-Regge approach, "PHC" for partonic and hadronic cascade, "Fact" for factorization approach.

Model	Theoretical concept	Flow	Ref.
EPOS3.076	GR	Hydro	This paper
EPOS LHC	GR	Parametrized	[53]
QGSJETII-04	GR	No	[51]
SIBYLL2.1	GR	No	[56]
PHOJET1.12A	GR	No	[57]
AMPT	PHC	Mo (in pp)	[52]
PYTHIA6.4.27	FACT	No	[58]
PYTHIA8.170	FACT	No	[59]
HERWIG++2.6.1A	FACT	No	[60]
SHERPA1.4.1	FACT	No	[61]

To answer this question, we investigate identified-particle production in EPOS3, compared to experimental data and many other models; see Table I. The QGSJETII [51], SIBYLL [56], and PHOJET model [57] are also based on Gribov-Regge multiple scattering, but there is no fluid component. The main ingredients of the AMPT model [52] are a partonic cascade and a subsequent hadronic cascade, providing in this way some "collectivity" in nuclear collisions, but not in proton-proton as studied here. EPOS LHC [53] is a tune of EPOS1.99, containing flow put in by hand, parametrizing the collective flow at freeze-out. The EPOS3 approach contains a full viscous hydrodynamical simulation. In addition, we also show results from the so-called "general-purpose event generators for LHC physics" [55], as there are PYTHIA6 [58], PYTHIA8 [59], HERWIG++ [60], and SHERPA [61]. All these models are based on the factorization formula for inclusive cross sections, with a more-or-less sophisticated treatment of multiple scattering, whereas Gribov-Regge theory provides a multiple scattering scheme from the beginning.

We have learned from studying identified-particle production in p-Pb scattering that hydrodynamic flow helps enormously to quantitatively reproduce experimental data, which show the typical "radial flow effect" of pushing intermediate p_t particles to higher p_t values, more and more pronounced with increasing particle mass. Huge effects are seen, for example, for lambdas. We will do the corresponding studies for proton-proton scattering at 7 TeV. In Fig. 26, we show the line

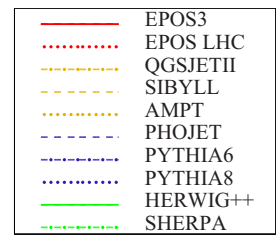

FIG. 26. (Color online) Line codes for the different models.

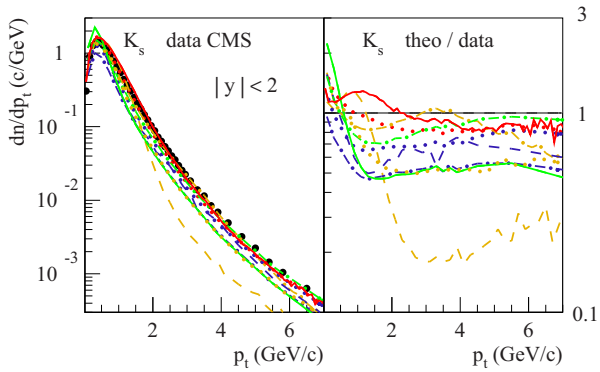

FIG. 27. (Color online) Transverse momentum spectra (left) and ratios "theory over data" (right) of K_s mesons in p-p scattering at 7 TeV. We show data from CMS [62] (symbols) and simulations from the different models, using the line codes defined in Fig. 26.

codes for the different models used in the following plots. In Fig. 27, we show the simulation results for K_s production compared to experimental data from CMS [62]. The best models are within 20% of the data; others are considerably below. In Fig. 28, we show the corresponding results for Λ and Ξ baryons, comparing simulations with data from CMS [62,63]. Here one can distinguish three groups of models. (1) QGSJETII and SIBYLL are far off the data; they are simply not constructed to produce these kind of baryons. (2) The so-called QCD generators like PYTHIA, HERWIG, SHERPA etc show a profound "dip" in the region between 1 and 5 GeV/c,

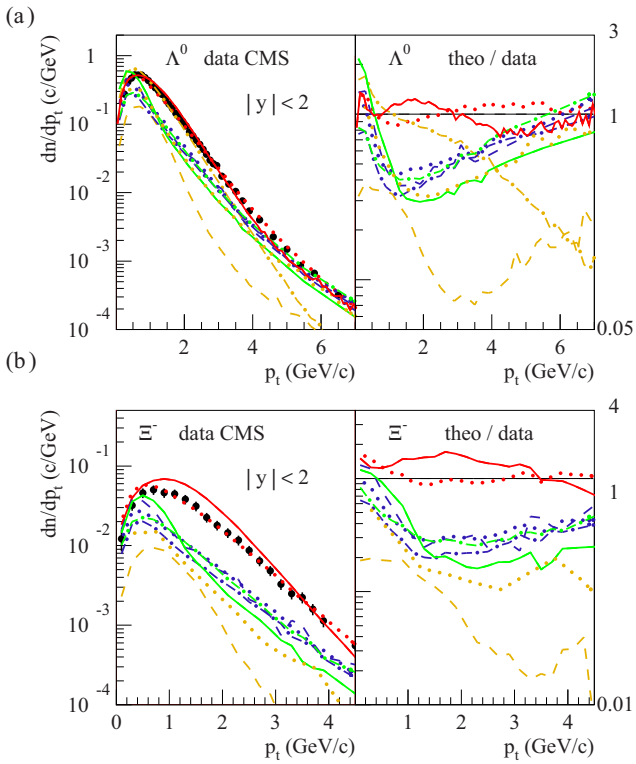

FIG. 28. (Color online) Same as Fig. 27, but here we plot results for Λ baryons (a) and Ξ baryons (b). CMS data from Refs. [62,63].

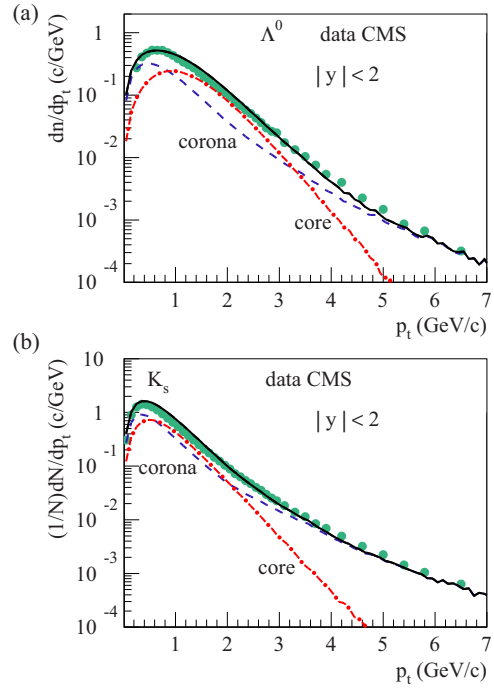

FIG. 29. (Color online) Transverse momentum spectra of Λ baryons (a) and K_s mesons (b) in p-p scattering at 7 TeV. We show data from CMS [62] (symbols) and simulations from EPOS3. The dashed lines are the corona contributions, the dash-dotted lines the core contributions, and the solid lines are the sums of all contributions.

underpredicting the data by a factor of 4–5 for the Ξ baryons and by a factor of around 3 for the Λ baryons. (3) The two EPOS versions are relatively close to the data. We recall that EPOS LHC contains collective flow (put in by hand) and EPOS3 hydrodynamic flow. In addition, particles are produced via statistical hadronization, which gives much higher yields for multistrange baryons, compared to string fragmentation, where these particles are highly suppressed.

From the above study we conclude that flow seems to help also in p-p scattering to explain particle spectra. To understand better the flow contribution, we plot in Fig. 29(a) again the transverse momentum spectra of Λ baryons, but this time only for EPOS3, also showing the corona and the core contribution. The core evolved hydrodynamically, and one can

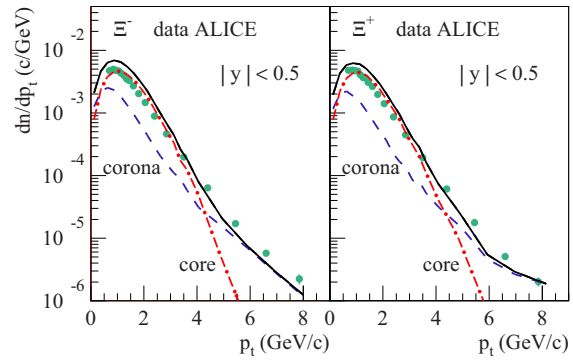

FIG. 30. (Color online) Same as Fig. 29, but here we plot results for Ξ^- and Ξ^+ baryons, compared to ALICE data [65].

see clearly the intermediate p_t enhancement owing to flow, as compared to "normal" production from (kinky) strings in the corona contributions. The same analysis for kaons in Fig. 29(b) shows that here the flow contribution is less prominent, owing to the typical flow feature that smaller masses (like kaons compared to lambdas) are less "pushed" to larger p_t values. So we get huge flow effects for heavy particles like Λ and Ξ baryons, as also seen in Fig. 30, where we compare the different contributions to Ξ baryon production to ALICE data [65].

XI. MULTIPLICITY-DEPENDENT PARTICLE PRODUCTION IN PROTON-PROTON SCATTERING AT 7 TeV

We discussed earlier the multiplicity dependence of particle production in p-Pb. The p_t spectra get systematically harder with multiplicity, and this effect is more pronounced for heavier particles. This is precisely what we get in a hydrodynamical scenario, and it even seems to work on a quantitative level.

Quite similar results (concerning the hardening of p_t spectra) have been obtained by the CMS collaboration for p-p scattering [64]. They performed a detailed study of the multiplicity dependence of (normalized) transverse momentum spectra. The multiplicity (referred to as N_{track} in Ref. [64]) counts the number of charged particles in the range $|\eta| < 2.4$. In our analysis we consider five multiplicity classes with mean values of 7, 40, 75, 98, and 131 in p-p scattering at 7 TeV.

In Fig. 31, we compare experimental data [64] for pions (black symbols) with the simulations from QGSJETII (top left panel), PYTHIA6 (top right), EPOS LHC (bottom left), and EPOS3 (bottom right). We use the tune Perugia 2011 (350) of PYTHIA6.4.27 (also in Figs. 32 and 33). The different curves in each figure refer to different centralities, with mean values

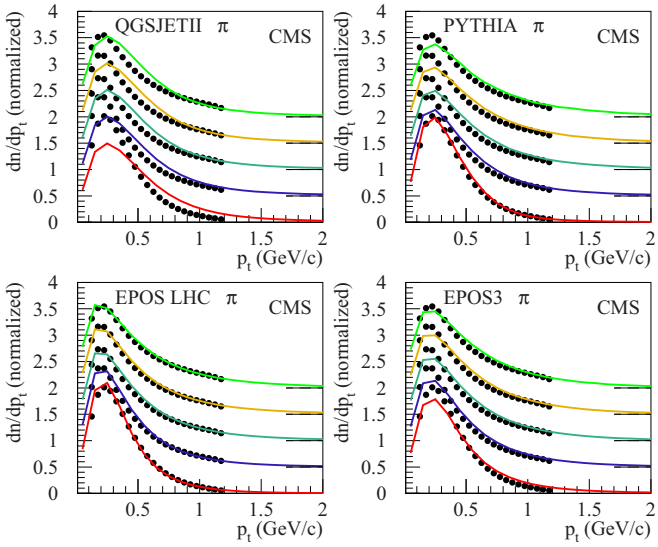

FIG. 31. (Color online) Transverse momentum spectra of pions in p-p scattering at 7 TeV, for five different multiplicity classes with mean values (from bottom to top) of 7, 40, 75, 98, and 131 charged tracks. We show data from CMS [64] (symbols) and simulations from QGSJETII, PYTHIA6, EPOS LHC, and EPOS3, as indicated in the figures.

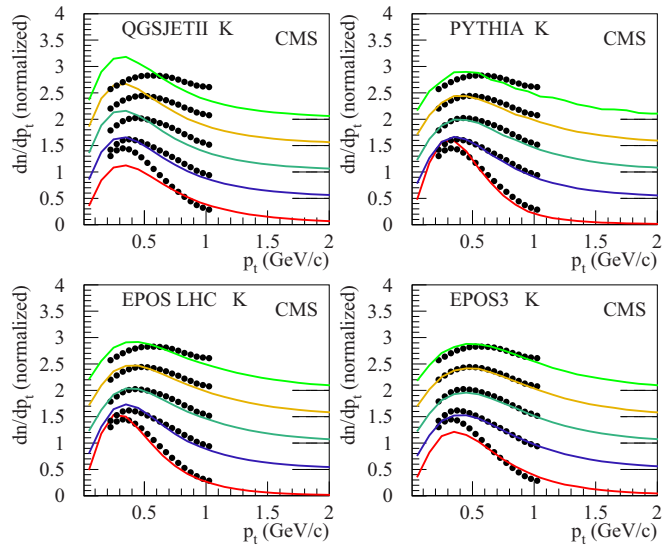

FIG. 32. (Color online) Same as Fig. 16, but for kaons.

(from bottom to top) of 7, 40, 75, 98, and 131 charged tracks. They are shifted relative to each other by a constant amount. Concerning the models, QGSJETII is the easiest to discuss, because here the curves for the different multiplicities are identical. The data, however, show a slight centrality dependence: The spectra get somewhat harder with increasing multiplicity. The other models, PYTHIA, EPOS LHC, and EPOS3 are close to the data. In Fig. 32, we compare experimental data [64] for kaons (black symbols) with the simulations. In the data, the shapes of the p_t spectra change considerably with multiplicity: They get much harder with increasing multiplicity. In QGSJETII, there is again no change, whereas PYTHIA, EPOS LHC, and EPOS show the right trend. EPOS3 reproduces better the high-multiplicity curves, PYTHIA and EPOS LHC the low-multiplicity results. In Fig. 33, we compare

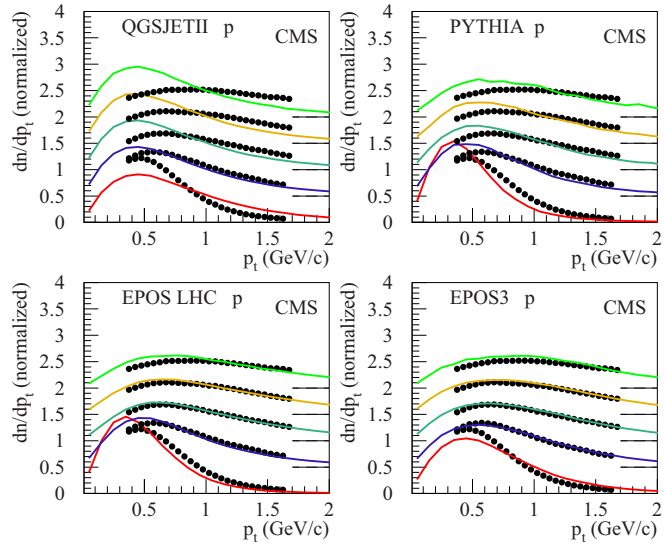

FIG. 33. (Color online) Same as Fig. 16, but for protons.

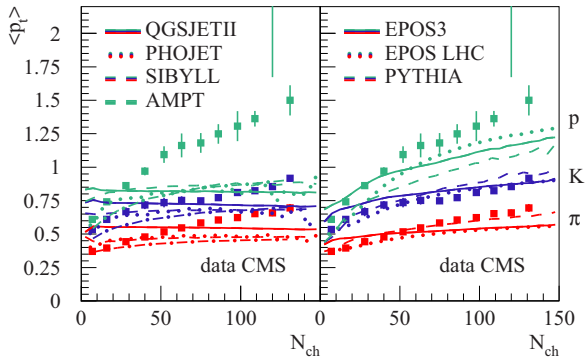

FIG. 34. (Color online) Multiplicity dependence of the average transverse momentum of protons (green), kaons (blue), and pions (red) in p-p scattering at 7 TeV. We show data from CMS [64] (symbols) and simulations from QGSJETII, PYTHIA6, EPOS LHC, EPOS3, and in addition PHOJET, SIBYLL, and AMPT.

experimental data [64] for protons (black symbols) with the simulations. Again, as for kaons, the experimental shapes of the p_t spectra change considerably, getting much harder with increasing multiplicity. In QGSJETII, the curves for the different multiplicities are identical. The PYTHIA model shows some change with multiplicity, but the shapes are not correct. EPOS LHC and EPOS3 give a reasonable description of the data. The hardening of the shapes with multiplicity, more and more pronounced with increasing particle mass, is here owing to the radial flow. *It seems that hydrodynamical flow again helps considerably to reproduce the data, even in proton-proton scattering*.

Based on these multiplicity-dependent p_t spectra, one obtains the multiplicity dependence of the average transverse momentum $\langle p_t \rangle$, as shown in Fig. 34, where we plot the multiplicity dependence of the average transverse momentum of protons (green), kaons (blue), and pions (red) in p-p scattering at 7 TeV. We show data from CMS [64] (symbols) and simulations from QGSJETII, PYTHIA6, EPOS LHC, EPOS3, and in addition PHOJET, SIBYLL, and AMPT. Whereas QGSJETII, PHOJET, SIBYLL, and AMPT show no or little multiplicity dependence, PYTHIA, EPOS LHC and EPOS3 increase with multiplicity, and this increase is more pronounced for heavier particles. In EPOS LHC and EPOS3, this is attributable to the radial flow, in PYTHIA owing to the so-called color reconnection.

XII. SUMMARY

We described in detail EPOS3, an event generator based on a 3D + 1 viscous hydrodynamical evolution starting from flux-tube initial conditions, generated in the Gribov-Regge multiple scattering framework. Individual scatterings are referred to as Pomerons, identified with parton ladders, eventually showing up as flux tubes (or strings). We discussed that in p-Pb collisions, the geometry is essentially determined by the number of Pomerons, being proportional to the number of flux tubes (and eventually to the multiplicity). A large number of flux tubes means a high probability to create high-density matter which will evolve hydrodynamically. This explains why in our approach with increasing multiplicity the hydrodynamical flow becomes more and more important, being visible in terms of a shift of intermediate p_t particles to higher values. This shift is more and more pronounced with increasing particle mass. These features seem to be present in recent p-Pb and even in p-p data. To confirm the "flow hypothesis," we compared EPOS3 simulations with essentially all available data on p_t spectra of identifies particles in p-Pb scattering at 5.02 TeV and p-p scattering at 7 TeV, and with all available simulations from other models. In all cases, hydrodynamical flow improves the situation considerably. It should be said that this is the first publication concerning EPOS3; the parameters are far from being optimized (it takes 1 month of simulations on several hundreds of nodes for one parameter set).

ACKNOWLEDGMENTS

This research was carried out within the scope of the GDRE (European Research Group) "Heavy ions at ultrarelativistic energies." Iu.K acknowledges support by the National Academy of Sciences of Ukraine (Agreement No. 2014) and by the State Fund for Fundamental Researches of Ukraine (Agreement No. 2014). Iu.K. acknowledges the financial support by Hessian initiative for excellence (LOEWE) through the Helmholtz International Center for FAIR (HIC for FAIR). B.G. acknowledges the financial support by the TOGETHER project of the Region of "Pays de la Loire."

[1] S. Chatrchyan *et al.* (CMS Collaboration), arXiv:1307.3442.
[2] B. Abelev *et al.* (ALICE Collaboration), Phys. Lett. B **728**, 25 (2014).
[3] H. J. Drescher, M. Hladik, S. Ostapchenko, T. Pierog, and K. Werner, Phys. Rep. **350**, 93 (2001).
[4] K. Werner, Iu. Karpenko, T. Pierog, M. Bleicher, and K. Mikhailov, Phys. Rev. C **82**, 044904 (2010).
[5] K. Werner, Iu. Karpenko, M. Bleicher, T. Pierog, and S. Porteboeuf-Houssais, Phys. Rev. C **85**, 064907 (2012).
[6] K. Werner, Iu. Karpenko, T. Pierog, M. Bleicher, and K. Mikhailov, Phys. Rev. C **83**, 044915 (2011).
[7] K. Werner and Iu. Karpenko, T. Pierog, Phys. Rev. Lett. **106**, 122004 (2011).
[8] P. Bozek and W. Broniowski, Phys. Rev. C **88**, 014903 (2013).
[9] A. Bzdak, B. Schenke, P. Tribedy, and R. Venugopalan, Phys. Rev. C **87**, 064906 (2013).
[10] G. Y. Qin and B. Mueller, Phys. Rev. C **89**, 044902 (2014).
[11] T. Regge, Nuovo Cim. **14**, 951 (1959).
[12] G. Chew and S. Frautsi, Phys. Rev. Lett. **7**, 394 (1961).
[13] R. Blankenbecler and M. Goldberger, Phys. Rev. **126**, 766 (1962).
[14] V. N. Gribov, Sov. Phys. JETP **14**, 1395 (1962).
[15] V. N. Gribov, I. Y. Pomeranchuk, and K. A. Ter-Martirosian, Yad. Fiz. (Russ.) **2**, 361 (1965).
[16] V. N. Gribov, Sov. Phys. JETP **26**, 414 (1968).
[17] V. N. Gribov and A. A. Migdal, Sov. J. Nucl. Phys. **8**, 583 (1969).

[18] V. N. Gribov and A. A. Migdal, Sov. Phys. JETP **28**, 784 (1969).
[19] V. N. Gribov, Sov. Phys. JETP **29**, 483 (1969).
[20] V. N. Gribov, Sov. Phys. JETP **30**, 709 (1970).
[21] V. A. Abramovskii, V. N. Gribov, and O. V. Kancheli, Sov. J. Nucl. Phys. **18**, 308 (1974).
[22] L. N. Lipatov, Sov. Phys. JETP **63**, 904 (1986).
[23] M. G. Ryskin and Y. M. Shabelski, Yad. Fiz. (Russ.) **55**, 2149 (1992).
[24] L. McLerran and R. Venugopalan, Phys. Rev. D **49**, 2233 (1994); **49**, 3352 (1994); **50**, 2225 (1994).
[25] I. Balitsky, Nucl. Phys. B **463**, 99 (1996).
[26] Yu. V. Kovchegov, Phys. Rev. D **60**, 034008 (1999).
[27] J. Jalilian-Marian, A. Kovner, A. Leonidov, and H. Weigert, Phys. Rev. D **59**, 014014 (1998); Nucl. Phys. B **504**, 415 (1997).
[28] E. Iancu, A. Leonidov, and L. D. McLerran, Phys. Lett. B **510**, 133 (2001); Nucl. Phys. A **692**, 583 (2001).
[29] H. Weigert, Nucl. Phys. A **703**, 823 (2002).
[30] K. Werner, F.-M. Liu, and T. Pierog, Phys. Rev. C **74**, 044902 (2006).
[31] Y. Nambu, *Proceedings of the International Conference on Symmetries and Quark Models, Wayne State University, 1969.*
[32] J. Scherk, Rev. Mod. Phys. **47**, 123 (1975).
[33] C. Rebbi, Phys. Rep. **12**, 1 (1974).
[34] X. Artru, Phys. Rep. **97**, 147 (1983).
[35] D. A. Morris, Nucl. Phys. B **288**, 717 (1987).
[36] M. Cacciari, G. Salam, and G. Soyez, J. High Energy Phys. 04 (2008) 063.
[37] (ATLAS Collaboration), Eur. Phys. J. C **71**, 1512 (2011).
[38] G. Aad *et al.* (ATLAS Collaboration), Phys. Rev. D **84**, 054001 (2011).
[39] Michal Vajzer (ALICE Collaboration), J. Phys. Conf. Ser. **446**, 012004 (2013).
[40] K. Werner, Phys. Rev. Lett. **98**, 152301 (2007).
[41] F. Becattini and J. Manninen, Phys. Lett. **B673**, 19 (2009).
[42] J. Aichelin and K. Werner, Phys. Rev. C **79**, 064907 (2009); **81**, 029902(E) (2010).
[43] J. Aichelin and K. Werner, J. Phys. **G37**, 094006 (2010).
[44] J. Aichelin and K. Werner, Phys. Rev. C **82**, 034906 (2010).
[45] M. Bleicher *et al.*, J. Phys. **G25**, 1859 (1999); H. Petersen, J. Steinheimer, G. Burau, M. Bleicher, and H. Stocker, Phys. Rev. C **78**, 044901 (2008).
[46] S. Borsanyi *et al.*, J. High Energy Phys. 11 (2010) 077.
[47] Y. Karpenko (private communication).
[48] W. Israel, Ann. Phys. **100**, 310 (1976); J. M. Stewart, Proc. R. Soc. London, Ser. A **357**, 59 (1977); W. Israel and J. M. Stewart, Ann. Phys. **118**, 341 (1979).
[49] M. Takamoto and S. Inutsuka, J. Comput. Phys. **230**, 7002 (2011).
[50] https://wiki.bnl.gov/TECHQM/index.php/Bulk_Evolution.
[51] S. Ostapchenko, Phys. Rev. D **74**, 014026 (2006); **83**, 014018 (2011).
[52] Z.-W. Lin, C. M. Ko, B.-A. Li, B. Zhang, and S. Pal, Phys. Rev. C **72**, 064901 (2005).
[53] T. Pierog, Iu. Karpenko, J. M. Katzy, E. Yatsenko, and K. Werner, arXiv:1306.5413.
[54] B. Abelev *et al.* (ALICE Collaboration), Phys. Rev. Lett. **110**, 082302 (2013).
[55] Andy Buckley *et al.*, Phys. Rep. **504**, 145 (2011).
[56] R. Engel, T. K. Gaisser, P. Lipari, and T. Stanev, *Proceedings of the 26th International Cosmic Ray Conference, Salt Lake City (USA)* (1999), p. 415; E.-J. Ahn, R. Engel, T. K. Gaisser, P. Lipari, and T. Stanev, Phys. Rev. D **80**, 094003 (2009).
[57] R. Engel, Z. Phys. C **66**, 203 (1995); R. Engel and J. Ranft, Phys. Rev. D **54**, 4244 (1996).
[58] T. Sjostrand, S. Mrenna, and P. Skands, J. High Energy Phys. 05 (2006) 026.
[59] T. Sjostrand, S. Mrenna, and P. Skands, Comput. Phys. Commun. **178**, 852 (2008).
[60] M. Bahr *et al.*, Eur. Phys. J. C **58**, 639 (2008).
[61] T. Gleisberg *et al.*, J. High Energy Phys. 02 (2009) 007.
[62] (CMS Collaboration), J. High Energy Phys. 05 (2011) 064.
[63] (CMS Collaboration), J. High Energy Phys. 05 (2011) 064.
[64] (CMS Collaboration), Eur. Phys. J. C **72**, 2164 (2012).
[65] B. Abelev *et al.* (ALICE Collaboration), Phys. Lett. B **712**, 309 (2012).